X. Wang, P. Xia, P. Masarati
Optimal Control of Pretwisted Rotating Thin-Walled Beams via Piezoelectrically Induced Couplings
AIAA Journal, Vol. 57, N. 6, 2019, p. 2617-2633
doi:10.2514/1.J058098

Optimal control of pretwisted rotating thin-walled beams via piezoelectrically induced couplings*

Xiao Wang† and Pinqi Xia‡
Nanjing University of Aeronautics and Astronautics, Nanjing, Jiangsu Province, 210016, China.

Pierangelo Masarati§
Politecnico di Milano, via La Masa, 34, 20156 Milano, Italy

Problems related to mathematical modeling and optimal active control of pretwisted adaptive blade are considered. The blade is modeled as a rotating thin-walled composite beam embedded with anisotropic piezo-composite layers accounting for nonclassical effects, such as transverse shear and warping inhibitions. The linear quadratic regulator feedback control strategy is adopted to study the tailoring of piezo-actuators on vibration suppression. Control authority of piezoelectrically induced transverse shear and bending coupling is highlighted. Tailoring studies using the present model reveal that piezoelectrically induced transverse shear plays an important role on control effectiveness. In addition, the relations between the control authority and the elastic couplings, piezoelectrically induced actuation couplings, pretwist angle, size and position of piezo-actuators are investigated.

Nomenclature

a_{ij}	1-D global stiffness coefficients
A_{ij}	Local stretching stiffness quantities of a wall
$\mathcal{A}_i^X$	Piezo-actuator coefficients
$2b$, $2d$	Width and depth of the box beam, see Fig. 2
b_{ij}	1-D mass coefficients
b_w	External bimoment per unit span
F_w, $a(s)$	Primary and secondary warping function, respectively
L	Length of the beam, see Fig. 2
$h(k)$	Thickness of the kth layer of a wall, see Eq. (15a)
J_{min}	Minimum cost function, see Eq. (37)
K_{ij}	Local stiffness coefficients

*Part of the manuscript was presented at 43^{rd} European Rotorcraft Forum, September 12-15, 2017, Milano, Italy
†Assistant Professor, National Key Laboratory of Rotorcraft Aeromechanics, College of Aerospace Engineer, No.29 Yudao St., Nanjing, China.
‡Full Professor, National Key Laboratory of Rotorcraft Aeromechanics, College of Aerospace Engineer, No.29 Yudao St., Nanjing, China.
§Full Professor, Dipartimento di Scienze e Tecnologie Aerospaziali, Politecnico di Milano, Italy

m_x, m_y, m_y	External moments per unit span
N_l	Number of the total layers in the wall, see Eq. (15a)
p_x, p_y, p_y	External forces per unit span
$P(y)$	Span distribution function, see Eq. (20)
R_0	Hub radius, see Fig. 1
(s, y, n)	Local coordinate system on the mid-line contour of the cross-section, see Fig. 2
(u_0, v_0, w_0)	Displacement components along x, y, z axes, see Fig. 2
V_i	Voltage parameters, see Eq. (21)
(x, y, z)	Rotating coordinate system at the blade root, see Fig. 1
(x_p, y_p, z_p)	Pretwist measurement coordinate system at the cross-section, see Fig. 2
α_K, α_M	Stiffness and mass weighting coefficients in state weighting matrix $\mathbf{Z}$ in Eq. (33)
$\beta(y)$	Pretwist angle
β_0, γ_0	Linear pretwist angle and presetting angle, see Eq. (38)
$\rho_{(k)}$	Mass density of the kth layer, see Eq. (15a)
η_i	Control weighting coefficients, see Eq. (33)
η_p, η_s	Position and size nondimensional parameters of piezo-actuator, see Eq. (42)
δ	Variation operator
δ_p, δ_s	1 or 0 tracers
θ_h, θ_p	Ply-angle of host structure and piezo-actuator, respectively
$(\theta_x, \theta_z, \phi)$	Rotations about the x, z and y axes, see Fig. 2
θ_p^F, θ_p^W	Ply-angle of flange and web actuator-pairs, respectively
$\mathbf{\Omega}$	Rotating speed
$\dot{()}, \ddot{()}, ()'$	$\partial()/\partial t, \partial^2()/\partial t^2, \partial()/\partial y$
$\mathbf{X}^T$	Transpose of the matrix or vector $\mathbf{X}$
$\oint_c, \int_0^L$	Integral along the cross-section and the span, respectively

I. Introduction

Because of the advantages with respect to weight criteria, specific high stiffness and elastic couplings, rotating composite thin-walled structures have a wide range of applications in various engineering structures, e.g., wind turbines, helicopter blades, and steam turbines. A large amount of work are devoted to the modeling and behavior investigation of composite rotor blades [1–11]. Recently, the blade incorporating adaptive materials technology into the host structure

are proposed for the design of new high performing blades [12–16]. In contrast to the passive control via tailoring technology, in those featuring adaptive capabilities, the frequencies, mode shapes and damping can be tuned to avoid structural resonance and to enhance dynamic response characteristics. Rafiee et al. [17] gave a comprehensive review of scholarly articles about dynamics, vibration and control of rotating composite beams and blades as published in the past decades. Because piezoelectric materials have a series of desirable characteristics, such as self-sensing, fast response and covering a broad range of frequencies, they are excellent candidates for the role of sensors and actuators, especially for the single crystal piezoceramics that can induce an order of magnitude larger than other piezoceramics [18]. In the last decades, piezoelectric fiber composite material, such as active fiber composite (AFC) [19] and macro fiber composite (MFC) [20] are introduced to overcome the drawbacks of the traditional monolithic piezoelectric materials, e.g., brittleness in nature, difficulty for embedding in curved surfaces. The significant benefits of piezoelectric composite materials, especially the widely used MFCs, are the orthotropic and anisotropic actuation capabilities, which allow more dirct and independent control of twist, bending, and extension [21].

In the existing literature, a lot publications on modeling or studying adaptive thin-walled structure activated via the piezoelectric patches [22–35]. Among them, Librescu and Song [22, 30] developed an adaptive thin-walled structure theory based on the assumption of the directions of piezoelectric patches are along the span; based on this model, Na et al. further considered the tapered cross-section [23], nonuniform effects [24] and active control of the thin-walled beam when implementing various modern control strategies [25, 26, 29]; Chandiramani et al. studied the optimal control of a rotating composite thin-walled beams via the piezoelectric patches [31] and further considered the variation of the electric field along the span [32]; Chattopadhyay et al. [33, 34] presented numerical results for the composite box-beam blade with self-sensing piezoelectric actuators, showing the nonlinear trade off between power consumption and vibration reduction; Wang et al. [35] extended the rotating thin-walled beam model developed by Libresu and Song via taking the anisotropic piezo-composite material into accounted and gave a comprehensive study allowing to get a better insight into the influence of piezoelectrically induced extension, transverse shear, twist, warping and bending actuations. Nevertheless, the literature devoted to the active control effectiveness of the rotating blades via the piezoelectrically induced actuation couplings is scarce. In other words, the influence of the synergistic effect on control authority when simultaneously implementing the elastic tailoring and the piezoelectric actuations tailoring is still not very clear. Thus, the objective of the present paper is trying to supply some pertinent information for this problem. In fact, a comprehensive study about the piezoelectrically induced actuation couplings on control effectiveness is a difficult task since the influences of a lot design factors should be taken into accounted, e.g., presetting and pretwist angles, elastic couplings, geometry of the blade, applied control strategy, voltages requirement, rotating speed, hub radius, sizes, positions and number of the piezo-actuators.

In this paper, based on the pretwisted adaptive rotating blade model developed in Ref. [35], the control authority on vibration suppression is investigated when implementing the Linear Quadratic Regular (LQR) optimal control

strategy to balance the control effectiveness and control energy consumption. The Extended Galerkin's Method (EGM) is used to semi-discretize the governing equation of the system for numerical study. The control effectiveness by piezoelectrically induced transverse shear is highlighted. The relations between the control authority and the elastic couplings, piezoelectrically induced actuation couplings, pretwist angle, size and position of piezo-actuators are investigated.

II. Basic assumptions and kinematics

A. Basic assumptions

The adaptive rotating blade that fixed on a rigid hub as shown in Fig. 1 is modeled as a fiber-reinforced composite thin-walled box beam bounded or embedded with anisotropic piezoelectric composite materials. Toward the modeling of the flexible rotating thin-walled beam structure, following assumptions are adopted [30, 35]:

1) the rotating speed is assumed as constant;
2) the cross-section is assumed preserved during deformation, but it allows warping out;
3) in additional to the primary warping on the mid-line contour, the off mid-line contour warping (referred to secondary warping) is also considered;
4) the transverse shear effect is taken into account;
5) the linear piezoelectric constitutive relationship is adopted for both fiber-reinforced and piezoelectric composite materials.

The mathematical modeling of the rotating thin-walled beam is actually based on the refined adaptive thin-walled beam theory developed in Ref. [35], in which the high speed rotation induced effects, such as centrifugal stiffening, Coriolis effect and tennis-racket effect [36] are specifically highlighted.

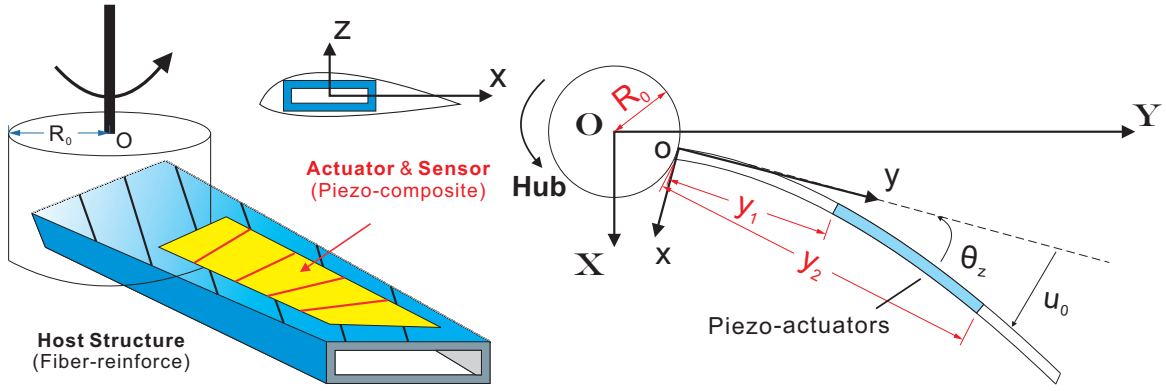

Fig. 1 A schematic description of the adaptive blade.

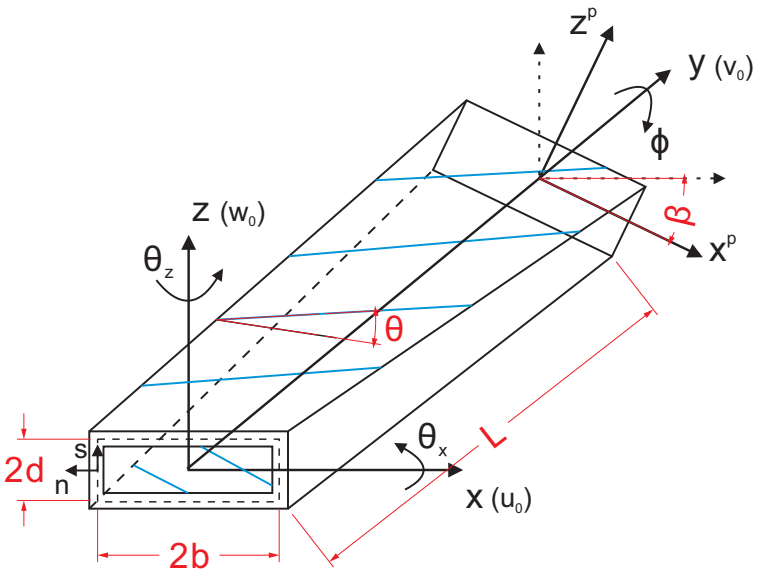

Fig. 2 Geometry of the pretwisted beam with a rectangular cross-section.

B. Kinematics

The rotating axis system (x, y, z) that located at the blade root with an offset R_0 from the rotation axis O is adopted to describe the deformation of the blade, see Figs. 1 and 2. The unit vectors of the (x, y, z) frame coordinate is defined as $(\mathbf{i}, \mathbf{j}, \mathbf{k})$. In addition, the other two surface coordinate systems attached on the cross-section are defined, i.e., pretwist measurement (x^p, y, z^p) and cross-section displacement description (s, y, n), see Fig. 2. Note that, coordinate system (s, y, n) is on the mid-line contour of the cross-section, while the coordinate systems (x^p, y, z^p) and (x, y, z) are related by the following transformation

$$\begin{cases} x(s, y) = x^p(s)\cos\beta(y) + z^p(s)\sin\beta(y), \\ z(s, y) = -x^p(s)\sin\beta(y) + z^p(s)\cos\beta(y), \end{cases} \tag{1}$$

where $\beta(y)$ denotes the pretwist angle.

It is beneficial to express the position vector $\mathbf{R}$ of an arbitrary point belonging to the deformed beam, measured from the fixed origin O (coinciding with the center of the hub), described in the rotating coordinate system (x, y, z), viz.,

$$\mathbf{R} = \mathbf{R}_0 + \mathbf{r} + \mathbf{D}, \tag{2}$$

where $\mathbf{R}_0$, $\mathbf{r}$ and $\mathbf{D}$ denote the position vector of the beam root point o (hub periphery), the undeformed position vector of the measured point, and its displacement vector, respectively. Their explicit expressions are

$$\mathbf{R}_0 = R_0\mathbf{j}, \qquad \mathbf{r} = x\mathbf{i} + y\mathbf{j} + z\mathbf{k}, \qquad \mathbf{D} = u\mathbf{i} + v\mathbf{i} + w\mathbf{k}, \tag{3}$$

where the components u, v and w in the displacement vector $\mathbf{D}$ are [37]

$$u(x,y,z,t) = u_0(x,t) + \left[z(s) + n\frac{\mathrm{d}\,x}{\mathrm{d}\,s}\right]\sin\phi(y,t) - \left[x(s) - n\frac{\mathrm{d}\,z}{\mathrm{d}\,s}\right][1-\cos\phi(y,t)], \tag{4a}$$

$$v(x,y,z,t) = v_0(y,t) + \left[x(s) - n\frac{\mathrm{d}\,z}{\mathrm{d}\,s}\right]\theta_z(y,t) + \left[z(s) + n\frac{\mathrm{d}\,x}{\mathrm{d}\,s}\right]\theta_x(y,t) - [F_w(s) + na(s)]\,\phi'(y,t), \tag{4b}$$

$$w(x,y,z,t) = w_0(y,t) - \left[x(s) - n\frac{\mathrm{d}\,z}{\mathrm{d}\,s}\right]\sin\phi(y,t) - \left[z(s) + n\frac{\mathrm{d}\,x}{\mathrm{d}\,s}\right][1-\cos\phi(y,t)]. \tag{4c}$$

$u_0(y,t)$, $v_0(y,t)$, $w_0(y,t)$, $\phi(y,t)$, $\theta_x(y,t)$, $\theta_z(y,t)$ in Eq. (4) represent the 1-D displacement measures as shown in Fig. 2, and are the basic unknown of the problem. The primary warping function $F_w(s)$ and the secondary warping function $na(s)$ are defined as

$$F_w(s) = \int_0^s [z\frac{\mathrm{d}\,x}{\mathrm{d}\,x} - x\frac{\mathrm{d}\,z}{\mathrm{d}\,s} - \psi(s)]\,\mathrm{d}\,s, \quad na(s) = -n(z\frac{\mathrm{d}\,z}{\mathrm{d}\,s} + x\frac{\mathrm{d}\,x}{\mathrm{d}\,s}). \tag{5}$$

As for the expression of the torsional function $\psi(s)$, one can refer to Refs. [38].

Based on the constant angular speed assumption, i.e., $\mathbf{\Omega} = \Omega\mathbf{k}$, the velocity vector of the arbitrary measured point can be given as:

$$\dot{\mathbf{R}}(x,y,z) = \dot{u}(x,y,z)\mathbf{i} - [R_0 + y + v(x,y,z)]\Omega\mathbf{i} + \dot{v}(x,y,z)\mathbf{j} + [x + u(x,y,z)]\Omega\mathbf{j} + \dot{w}\mathbf{k}. \tag{6}$$

C. Strains

The strains that contribute to the potential energy are presented.

Spanwise strain

$$\varepsilon_{yy}(n,s,y,t) = \varepsilon^0_{yy}(s,y,t) + n\varepsilon^1_{yy}(s,y,t), \tag{7}$$

where ε^0_{yy} denotes the axial strain associated with the primary warping and ε^1_{yy} denotes a measure of curvature associated with the secondary warping, viz.,

$$\varepsilon^0_{yy} = \left[v_0' + x\theta_z' + z\theta_x' - F_w\phi''\right] + \frac{1}{2}\left[(u_0')^2 + (w_0')^2 + (x^2+z^2)\phi'^2\right] + u_0'\phi'(z\cos\phi - x\sin\phi) - w_0'\phi'(x\cos\phi + z\sin\phi), \tag{8a}$$

$$\varepsilon^1_{yy} = -\frac{\mathrm{d}\,z}{\mathrm{d}\,s}\theta_z' + \frac{\mathrm{d}\,x}{\mathrm{d}\,s}\theta_x' - a\phi'' + \phi'\left[u_0'\left(\frac{\mathrm{d}\,x}{\mathrm{d}\,s}\cos\phi + \frac{\mathrm{d}\,z}{\mathrm{d}\,s}\sin\phi\right) + w_0'\left(\frac{\mathrm{d}\,z}{\mathrm{d}\,s}\cos\phi - \frac{\mathrm{d}\,x}{\mathrm{d}\,s}\sin\phi\right) + r_n\phi'\right]. \tag{8b}$$

Tangential shear strain:

$$\gamma_{sy}(s,y,t) = \gamma^0_{sy}(s,y,t) + \psi(s)\phi'(y,t) + 2n\phi', \tag{9}$$

where

$$\gamma_{sy}^{0} = \frac{\mathrm{d}\,x}{\mathrm{d}\,s}\left(\theta_z + u_0' \cos\phi - w_0' \sin\phi\right) + \frac{\mathrm{d}\,z}{\mathrm{d}\,s}\left(\theta_x + u_0' \sin\phi + w_0' \cos\phi\right). \tag{10}$$

Transverse shear stain:

$$\gamma_{ny} = \frac{\mathrm{d}\,x}{\mathrm{d}\,s}\left(\theta_x + u_0' \sin\phi + w_0' \cos\phi\right) - \frac{\mathrm{d}\,z}{\mathrm{d}\,s}\left(\theta_z + u_0' \cos\phi - w_0' \sin\phi\right). \tag{11}$$

D. Constitutive relations

The fiber-reinforced composite material constituting the host structure and the piezo-composite material (e.g. MFC [39]) playing the role of actuator can both be modeled using the linear piezoelectric constitutive equation [35, 37]. The stress resultants and stress couples can reduce to the following expressions

$$\begin{Bmatrix} N_{yy} \\ N_{ys} \\ L_{yy} \\ L_{sy} \end{Bmatrix} = \begin{bmatrix} K_{11} & K_{12} & K_{13} & K_{14} \\ K_{21} & K_{22} & K_{23} & K_{24} \\ K_{41} & K_{42} & K_{43} & K_{44} \\ K_{51} & K_{52} & K_{53} & K_{54} \end{bmatrix} \begin{Bmatrix} \epsilon_{yy}^{0} \\ \gamma_{ys}^{0} \\ \phi' \\ \epsilon_{yy}^{1} \end{Bmatrix} - \begin{Bmatrix} \tilde{N}_{yy} \\ \tilde{N}_{sy} \\ \tilde{L}_{yy} \\ \tilde{L}_{sy} \end{Bmatrix}, \tag{12}$$

and

$$N_{yn} = \left(A_{44} - \frac{{A_{45}}^2}{A_{55}}\right)\gamma_{yn}. \tag{13}$$

The explicit expressions of the local stiffness coefficients K_{ij} and the stretching stiffness quantities A_{ij} are given in Ref. [37]. While the piezoelectrically induced stress resultant components $\tilde{N}_{yy}$, $\tilde{N}_{sy}$ and stress couple components $\tilde{L}_{yy}$, $\tilde{L}_{sy}$ are given in Refs. [35, 40].

III. Formulation of the governing system

The governing equations and the associated boundary conditions are derived from Hamilton's principle. This can be stated as

$$\int_{t_0}^{t_1} \left[\delta T + \delta W_e - \delta U\right] \mathrm{d}\,t = 0, \tag{14}$$

where the kinetic energy T, the elastic energy U and the virtual work of the external loads on the blade W_e can be given as

$$T = \frac{1}{2}\int_0^L \oint_c \sum_{k=1}^{N_l} \int_{h(k)} \rho\,(k)(\dot{\mathbf{R}} \cdot \dot{\mathbf{R}})\,\mathrm{d}\,n\,\mathrm{d}\,s\,\mathrm{d}\,y, \tag{15a}$$

$$U = \frac{1}{2}\int_0^L \oint_c \left[N_{yy}\varepsilon^0_{yy} + N_{ys}\gamma^0_{sy} + L_{yy}\varepsilon^1_{yy} + L_{sy}\phi' + N_{ny}\gamma_{ny}\right] \mathrm{d}\, s\, \mathrm{d}\, y, \tag{15b}$$

$$W_e = \int_0^L \left[p_x u_0 + p_y v_0 + p_z w_0 + m_x\theta_x + (m_y + b_w{}')\phi + m_z\theta_z\right] \mathrm{d}\, y. \tag{15c}$$

In Eqs. (14) and (15), t_0 and t_1 denote two arbitrary motions of time; $\rho(k)$ denotes the mass density of the kth layer; N_{hp} is the total number of the layers; L is the length of the blade; p_x, p_y, p_z, m_x, m_y, m_z and b_w are the external excitation per unit span length; while δ and $(\,)'$ denote the variation operator and $\partial()/\partial y$, respectively.

For the general case of ply-up configuration, the system exhibits a complete coupling between the various modes, that is, warping (primary and secondary), bending (flapping and lagging), transverse shearing (chordwise and flapwise), twist and extension. In engineering applications, special lay-up configuration is normally adopted to design particular couplings [41]. Here, *circumferentially uniform stiffness* (CUS) configuration [42] is considered. For the pretwisted thin-walled beam with rectangular cross-section as shown in Fig. 2, CUS configuration implies the ply-angle distribution $\theta(z_p) = \theta(-z_p)$ of the top and bottom walls and $\theta(x_p) = \theta(-x_p)$ of the left and right walls. Indicated in Ref. [35], this configuration will decouple the system into two independent subsystems, i.e., one governs the flapping-lagging coupling motion ($u_0 - w_0 - \theta_x - \theta_z$) and the other governs the twist-extension coupling motion ($v_0 - \phi$). The present article is focused on the former subsystem considering the fact that the active twist control of the more straightforward twist-extension subsystem has been widely investigated, e.g., Refs. [12, 35].

After a lengthy variation process of Eq. (14), the governing equations expressed in terms of displacement quantities by ignoring the immaterial nonlinear terms are

$$\delta u_0 \,:\, a_{34}\theta_x'' + a_{44}(u_0'' + \theta_z') + p_x + \underline{b_1\Omega^2[R(y)u_0']'} - b_1[\ddot{u}_0 - \underbrace{2\Omega\dot{v}_0}_{\sim\sim} - \underline{\Omega^2 u_0}] + \delta_p \mathcal{A}_1^{Qx} V_1 P'(y) = 0, \tag{16a}$$

$$\delta w_0 \,:\, a_{25}\theta_z'' + a_{55}(w_0'' + \theta_x') + \underline{b_1\Omega^2[R(y)w_0']'} - b_1\ddot{w}_0 + p_z + \delta_p \mathcal{A}_3^{Qz} V_3 P'(y) = 0, \tag{16b}$$

$$\begin{aligned}\delta\theta_x \,:\, & a_{33}\theta_x'' + a_{34}(u_0'' + \theta_z') - a_{25}\theta_z' - a_{55}(w_0' + \theta_x) + m_x - b_4\ddot{\theta}_x - b_6\ddot{\theta}_z \\ & - \underbrace{2\Omega b_4\dot{\phi}}_{\sim\sim} + \underline{\underline{\Omega^2(b_4\theta_x + b_6\theta_z)}} + \delta_p \mathcal{A}_1^{Mx} V_1 P'(y) - \mathcal{A}_3^{Qz} V_3 P(y) = 0,\end{aligned} \tag{16c}$$

$$\begin{aligned}\delta\theta_z \,:\, & a_{22}\theta_z'' + a_{25}(w_0'' + \theta_x') - a_{34}\theta_x' - a_{44}(u_0' + \theta_z) + m_z - b_5\ddot{\theta}_z - b_6\ddot{\theta}_x - \underbrace{2\Omega b_6\dot{\phi}}_{\sim\sim} \\ & + \underline{\underline{\Omega^2(b_5\theta_z + b_6\theta_x)}} + \delta_p \mathcal{A}_3^{Mz} V_3 P'(y) - \mathcal{A}_1^{Qx} V_1 P(y) = 0.\end{aligned} \tag{16d}$$

The associated boundary conditions at the blade root $y = 0$ are

$$u_0 = w_0 = \theta_x = \theta_z = 0, \tag{17}$$

and at the blade tip $y = L$ are

$$\delta u_0 \ : a_{24}(L)\theta_z' + a_{34}(L)\theta_x' + a_{44}(L)(u_0' + \theta_z) + a_{45}(L)(w_0' + \theta_x) + \delta_s \left[\mathcal{A}_1^{Qx} V_1 \cos\beta(L) + \mathcal{A}_3^{Qz} V_3 \sin\beta(L)\right] = 0, \tag{18a}$$

$$\delta w_0 \ : a_{25}(L)\theta_z' + a_{35}(L)\theta_x' + a_{45}(L)(u_0' + \theta_z) + a_{55}(L)(w_0' + \theta_x) + \delta_s \left[\mathcal{A}_3^{Qz} V_3 \cos\beta(L) - \mathcal{A}_1^{Qx} V_1 \sin\beta(L)\right] = 0, \tag{18b}$$

$$\delta\theta_x \ : a_{23}(L)\theta_z' + a_{33}(L)\theta_x' + a_{34}(L)(u_0' + \theta_z) + a_{35}(L)(w_0' + \theta_x) + \delta_s \left[\mathcal{A}_1^{Mx} V_1 \cos\beta(L) - \mathcal{A}_3^{Mz} V_3 \sin\beta(L)\right] = 0, \tag{18c}$$

$$\delta\theta_z \ : a_{22}(L)\theta_z' + a_{23}(L)\theta_x' + a_{24}(L)(u_0' + \theta_z) + a_{25}(L)(w_0' + \theta_x) + \delta_s \left[\mathcal{A}_3^{Mz} V_3 \cos\beta(L) + \mathcal{A}_1^{Mx} V_1 \sin\beta(L)\right] = 0. \tag{18d}$$

In these equations

$$R(y) = R_0(L - y) + \frac{1}{2}(L^2 - y^2), \tag{19}$$

$a_{ij}(y)$, $b_{ij}(y)$ and $\mathcal{A}_i^X$ are the stiffness, mass and piezo-actuator coefficients, respectively. Their explicit expressions are given in Refs. [37] and [40], respectively. $P(y)$ denotes the span location of the piezo-actuator as shown in Fig. 1

$$P(y) = H(y - y_1) - H(y - y_2), \tag{20}$$

where $H(\cdot)$ is Heaviside's distribution. For the cases (i) the actuator is spread over the entire beam span and (ii) the actuator is a single patch, the traces have to be taken as (i) $\delta_p = 0$ and $\delta_s = 1$ and (ii) $\delta_p = 1$ and $\delta_s = 0$, respectively. In fact, the piezo-actuators can be split into two individual actuator-pairs, viz., flange-actuator-pair (top and bottom) and web-actuator-pair (left and right) as shown in Fig. 3. Voltage parameters V_1 and V_3 that contributed by the flange-actuator-pair and the web-actuator-pair are defined in sequence as

$$V_1 = \frac{V_T - V_B}{2}, \qquad V_3 = \frac{V_L - V_R}{2}, \tag{21}$$

where V_T, V_B, V_L and V_R are the voltages applied on the top, bottom, left and right walls, respectively, see Fig. 3. Note that, the terms in the governing equations (16) associated with (i) the centrifugal acceleration, (ii) the Coriolis and (iii) the centrifugal-rotatory effects are underscored by (i) a solid line (____), (ii) a wavy line (____) and (iii) two superposed solid lines (____), respectively. One can refer to, e.g., Refs. [8, 36, 41] for more details of thesis high rotating speed induced effects.

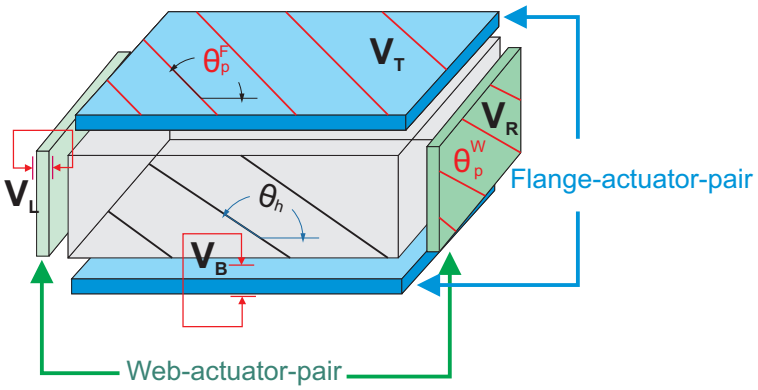

Fig. 3 Piezo-actuator configuration.

In addition, a special case, the untwisted rotor blade with host structure fiber orientation along the span ($\theta_h = 90°$) is highlighted. It can be verified that the stiffness coefficients a_{23}, a_{24}, a_{25}, a_{34}, a_{35}, a_{45} and the mass coefficient b_6 all equal to zero in the governing equations (16) and the associated natural boundary conditions (18). As a result, the flapping and the lagging motions can be completely decoupled, i.e., the governing equations for lagging motion are

$$\delta u_0 \ : a_{44}(u_0'' + \theta_z') + p_x + \underline{b_1\Omega^2[R(y)u_0']'} - b_1[\ddot{u}_0 - \underline{\Omega^2 u_0}] + \delta_p \mathcal{A}_1^{Qx} V_1 P'(y) = 0, \tag{22a}$$

$$\delta\theta_z \ : a_{22}\theta_z'' - a_{44}(u_0' + \theta_z) + m_z - b_5\ddot{\theta}_z + \underline{\underline{\Omega^2 b_5\theta_z}} + \delta_p \mathcal{A}_3^{Mz} V_3 P'(y) - \mathcal{A}_1^{Qx} V_1 P(y) = 0, \tag{22b}$$

with the natural boundary conditions as

$$\delta u_0 \ : a_{44}(u_0' + \theta_z) + \delta_s \mathcal{A}_1^{Qx} V_1 = 0, \tag{23a}$$

$$\delta\theta_z \ : a_{22}\theta_z' + \delta_s \mathcal{A}_3^{Mz} V_3 = 0; \tag{23b}$$

while the governing equations for flapping motion are

$$\delta w_0 \ : a_{55}(w_0'' + \theta_x') + \underline{b_1\Omega^2[R(y)w_0']'} - b_1\ddot{w}_0 + p_z + \delta_p \mathcal{A}_3^{Qz} V_3 P'(y) = 0, \tag{24a}$$

$$\delta\theta_x \ : a_{33}\theta_x'' - a_{55}(w_0' + \theta_x) + m_x - b_4\ddot{\theta}_x + \underline{\underline{\Omega^2 b_4\theta_x}} + \delta_p \mathcal{A}_1^{Mx} V_1 P'(y) - \mathcal{A}_3^{Qz} V_3 P(y) = 0, \tag{24b}$$

with the natural boundary conditions are

$$\delta w_0 \ : a_{55}(w_0' + \theta_x) + \delta_s \mathcal{A}_3^{Qz} V_3 = 0, \tag{25a}$$

$$\delta\theta_x \ : a_{33}\theta_x' + \delta_s \mathcal{A}_1^{Mx} V_1 = 0. \tag{25b}$$

IV. Solution methodology

A. The Extend Galerkin's Method

The Extend Galerkin's Method (EGM) [43] is applied to discretize the system for numerical study. The basic idea of EGM is to select the appropriate shape functions that exactly satisfy only the geometric boundary conditions. The residual terms resulting from the non-fulfillment of natural boundary conditions are then minimized in the Galerkin sense [44]. We assume

$$u_0(y,t) = \mathbf{\Psi}_u^T(y)\mathbf{q}_u(t), \quad w_0(y,t) = \mathbf{\Psi}_w^T(y)\mathbf{q}_w(t), \quad \theta_x(y,t) = \mathbf{\Psi}_x^T(y)\mathbf{q}_x(t), \quad \theta z(y,t) = \mathbf{\Psi}_z^T(y)\mathbf{q}_z(t), \tag{26}$$

where the shape functions $\mathbf{\Psi}_u^T(y)$, $\mathbf{\Psi}_w^T(y)$, $\mathbf{\Psi}_x^T(y)$ and $\mathbf{\Psi}_z^T(y)$ are required to fulfill the geometric boundary conditions. Thus the discretized forms of the system when ignoring the Coriolis terms which are immaterial for small thickness ratio blade [45] follow as

$$\mathbf{M}\ddot{\mathbf{q}} + [\mathbf{K} + \Omega^2\hat{\mathbf{K}}]\mathbf{q} + \mathcal{A}_\mathbf{1} V_1 + \mathcal{A}_\mathbf{3} V_3 = \mathbf{Q}, \tag{27}$$

where

$$\mathbf{q} = \begin{Bmatrix} \mathbf{q}_u^T & \mathbf{q}_w^T & \mathbf{q}_x^T & \mathbf{q}_z^T \end{Bmatrix}^T. \tag{28}$$

The expressions for mass matrix $\mathbf{M}$, stiffness matrix $\mathbf{K}$, dynamical stiffness matrix $\hat{\mathbf{K}}$, piezo-actuator vector $\mathcal{A}_\mathbf{i}$ and external excitation vector $\mathbf{Q}$ are given in appendix of Ref. [35].

B. Linear quadratic regulator optimal control

One important target of the piezo-actuators is to suppress the vibration of the blade. To achieve this target, linear quadratic regulator (LQR) optimal control based on the use of a full state feedback scheme is adopted. Therefore, Eq. (27) can be cast in state-space form as

$$\dot{\mathbf{x}}(t) = \mathbf{A}\mathbf{x}(t) + \mathbf{B}\mathbf{Q}(t) - \mathbf{B}\mathcal{A}_\mathbf{1} V_1(t) - \mathbf{B}\mathcal{A}_\mathbf{3} V_3(t), \tag{29}$$

where

$$\mathbf{x}(t) = \begin{bmatrix} \mathbf{q}^T(t) \\ \dot{\mathbf{q}}^T(t) \end{bmatrix}, \quad \mathbf{A} = \begin{bmatrix} \mathbf{0} & \mathbf{I} \\ -\mathbf{M}^{-1}\mathbf{K} & \mathbf{0} \end{bmatrix}, \quad \mathbf{B} = \begin{Bmatrix} \mathbf{0} \\ \mathbf{M}^{-1} \end{Bmatrix}. \tag{30}$$

Note that the LQR control provides sort of a benchmark, an ideal optimal value which cannot be obtained in practical applications because the state $\mathbf{x}$ is not available and needs to be reconstructed using a state estimator that degrades the

quality of the regulator. Within the LQR control algorithm, minimizing the response of the closed-loop rotating blade system and the piezo-actuator control effort at the same time, the following cost function is adopted

$$J = \frac{1}{2}\int_{t_0}^{t_f} \left(\mathbf{x}^T \mathbf{Z}\mathbf{x} + V_i R_i V_i\right) \mathrm{d}\, t, \tag{31}$$

where t_0 and t_f denote the present and the final time, respectively. The state weighting matrix $\mathbf{Z}$ and the control weighting scalar R_i should be positive semidefinite and positive definite, respectively. According to Ref. [46], following

$$\mathbf{Z} = \begin{bmatrix} \alpha_K \mathbf{K} & \mathbf{0} \\ \mathbf{0} & \alpha_M \mathbf{M} \end{bmatrix}, \quad R_i = \eta_i \mathcal{A}_\mathbf{i}{}^T \mathbf{K}^{-1} \mathcal{A}_\mathbf{i}, \quad (i = 1, 3) \tag{32}$$

are adopted for to make a trade off between control effectiveness and additional energy consumption, namely of minimizing the response with that of minimizing the control effort. The stiffness and mass weighting coefficients α_K and α_M in Eq. (32) are non-negative scalars, while the control weighting coefficients η_i are positive scalars. The matrix $\mathbf{Z}$ actually represents the sum of the system kinetic and potential energies in the sense of

$$\frac{1}{2}\int_{t_0}^{t_f} \mathbf{x}^T \mathbf{Z}\, \mathrm{d}\, t = \frac{1}{2}\int_{t_0}^{t_f} \left[\alpha_M \dot{\mathbf{q}}^T \mathbf{M}\dot{\mathbf{q}} + \alpha_K \mathbf{q}^T \mathbf{K}\mathbf{q}\right] \mathrm{d}\, t. \tag{33}$$

Thus the feedback control law that minimizes the value of the cost is

$$V_i(t) = -\mathbf{G}_i \mathbf{x}(t), \quad (i = 1, 3) \tag{34}$$

where

$$\mathbf{G}_i = -\mathbf{R}^{-1} \mathcal{A}_\mathbf{i}{}^T \mathbf{B}^T \mathbf{P}_\mathbf{i}, \tag{35}$$

is the optimal gain matrix, while $\mathbf{P_i}$ is the positive-definite solution to the following steady-state Riccati equation

$$\mathbf{Z} + \mathbf{P_i}\mathbf{A} + \mathbf{A}^T \mathbf{P_i} - R_i \mathbf{P_i} \mathbf{B} \mathcal{A}_\mathbf{i} \mathcal{A}_\mathbf{i}{}^T \mathbf{B}^T \mathbf{P_i} = 0. \tag{36}$$

The associated minimum solution of the cost function J_{min} can be given as

$$J_{min} = \frac{1}{2}\mathbf{x}^T(t_0)\mathbf{P_i}\mathbf{x}(t_0). \tag{37}$$

V. Numerical study and discussion

The geometric specifications and the material properties of the host structure of the thin-walled box beam used in numerical study are shown in Table 1. While the material properties of the piezo-actuators are specified in Table 2. The details of the lay-up configurations of the blade are listed in Table 3. Validations of the present thin-walled beam model have been performed in Refs. [35, 40]. Note that, in this numerical study, unless otherwise stated, the following assumptions are adopted.

1) The linear pretwist angle

$$\beta(y) = \gamma_0 - \beta_0 \frac{y}{L} \tag{38}$$

is accounted. In addition, the presetting angle $\gamma_0 = \beta_0$ is further assumed to make the pretwist angle at the beam tip equal to zero. As a result, Eq. (38) can be further expressed as

$$\beta(y) = \frac{L - y}{L} \beta_0. \tag{39}$$

2) The piezo-actuators are assumed bonded outside the host structure.

3) Radius of the hub is assumed as $R_0 = 0.1L$ and the constant rotating speed is assumed as $\Omega = 1000$ rpm.

Table 1 Material properties (Graphite-Epoxy) and geometric specifications of the host structure

Material	**Value**	**Geometric**	**Value**
E_{11}	206.8×10^9 N $\cdot$ m^{-2}	Width ($2b$[a])	0.254 m
$E_{22} = E_{33}$	5.17×10^9 N $\cdot$ m^{-2}	Depth ($2d$[a])	0.0681 m
$G_{13} = G_{23}$	2.55×10^9 N $\cdot$ m^{-2}	Hub radius (R_0)	0.2032 m
G_{12}	3.10×10^9 N $\cdot$ m^{-2}	Number of layers	6
$\mu_{12} = \mu_{13} = \mu_{23}$	0.25	Layer thickness	0.0017 m
ρ	1.528×10^3 Kg $\cdot$ m^{-3}	Length (L)	2.032 m

[a]The length is measured on the mid-line contour.

Table 2 Material properties of piezo-actuator [47]

E_{11}	31.28×10^9 N $\cdot$ m^{-2}	d_{11}	386.63×10^{-12} m $\cdot$ V^{-1}
$E_{22} = E_{33}$*	17.05×10^9 N $\cdot$ m^{-2}	$d_{12} = d_{13}$*	-175.50×10^{-12} m $\cdot$ V^{-1}
$G_{12} = G_{13}$* $= G_{23}$*	5.12×10^9 N $\cdot$ m^{-2}	ρ	5.1159×10^3 Kg $\cdot$ m^{-3}
$\mu_{12} = \mu_{13}$* $= \mu_{23}$*	0.303	Number of layers	1
Electrode spacing [48]	0.4318 mm	Thickness [48]	0.1905 mm

* The value is assumed by the author.

Table 3 CUS lay-up configurations of the thin-walled box beam

		Flanges		Webs	
Layer	Material	Top	Bottom	Left	Right
CUS (1-6)	Host structure	$[\theta_h]_6$	$[\theta_h]_6$	$[\theta_h]_6$	$[\theta_h]_6$
CUS (7)	Piezo-actuator	$[\theta_p^F]$	$[\theta_p^F]$	$[\theta_p^W]$	$[\theta_p^W]$

A. Study of piezo-actuator coefficients

Since the values of the piezo-actuator coefficients in the present system are proportional to the circumference size [35, 40], we assume the piezo-actuators are spread over the entire cross-section to obtain the maximum piezoelectrically induced actuations. Fig. 4 highlights the influences contributed by the additional mass and stiffness of the piezo-actuators on frequencies. Fig. 4a plots frequencies of the first four modes as a function of the host structure ply-angle θ_h, comparing the solution without the effects of mass and stiffness of the piezo-actuator (indicated by solid lines) and the solution with them (indicated by dashed lines). It can be found that ignoring them solely results in less than 6% error considering in conjunction with the results as shown in Fig. 4b. As a result, since the main objective of the present investigation is to highlight the control authority via tailoring the piezo-composite layers, the effect of mass and stiffness of the piezo-actuators can be safely ignored here for simplification [44].

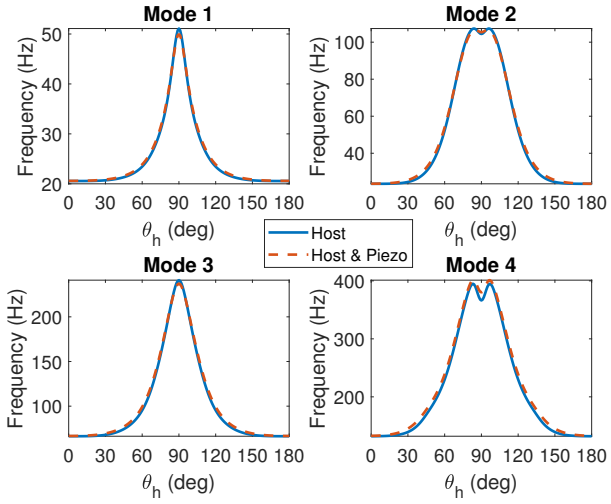

(a) Frequencies of the first four modes; $\theta_p^F = \theta_p^W = \theta_h$.

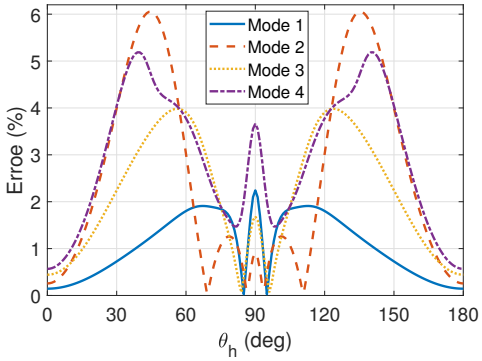

(b) Errors when the effects of mass and stiffness of the piezo-actuators are ignored; ($error = \left|\frac{[Host] - [Host\&Piezo]}{[Host\&Piezo]} \times 100\%\right|$).

Fig. 4 The influences of mass and stiffness of the piezo-actuators.

The piezo-actuator coefficients induced by flange-actuator-pair and web-actuator-pair are illustrated in Fig. 5 by solid and dashed lines, respectively. It can be found that transverse shear coefficients $\mathcal{A}_1^{Qx}$ (chordwise) and $\mathcal{A}_3^{Qz}$ (flapwise) in Fig. 5a show a anti-symmetric dependence centered around $\theta_p = 90°$, while bending coefficients $\mathcal{A}_1^{Mx}$ (flapwise) and $\mathcal{A}_3^{Mz}$ (chordwise) in Fig. 5b present the symmetric property. In addition, the pure bending actuation points

($\mathcal{A}_1^{Qx} = \mathcal{A}_3^{Qz} = 0$) are indicated by $\triangle$ in Fig. 5a, while the pure transverse shear actuation points ($\mathcal{A}_1^{Mx} = \mathcal{A}_3^{Qz} = 0$) are specified by $\circ$ in Fig. 5b.

In a nutshell, when $\theta_p^F = \theta_p^W = 90°$, piezo-actuators will produce the maximum piezoelectrically induced bending moment and the associated shear actuations are immaterial. Nevertheless, when the piezo-actuators provide maximum piezoelectrically induced transverse shears at $\theta_p^F = \theta_p^W \approx 53°$ or $127°$ (indicated by $\times$ in Fig. 5a), the system is also controlled by adequate bending actuations.

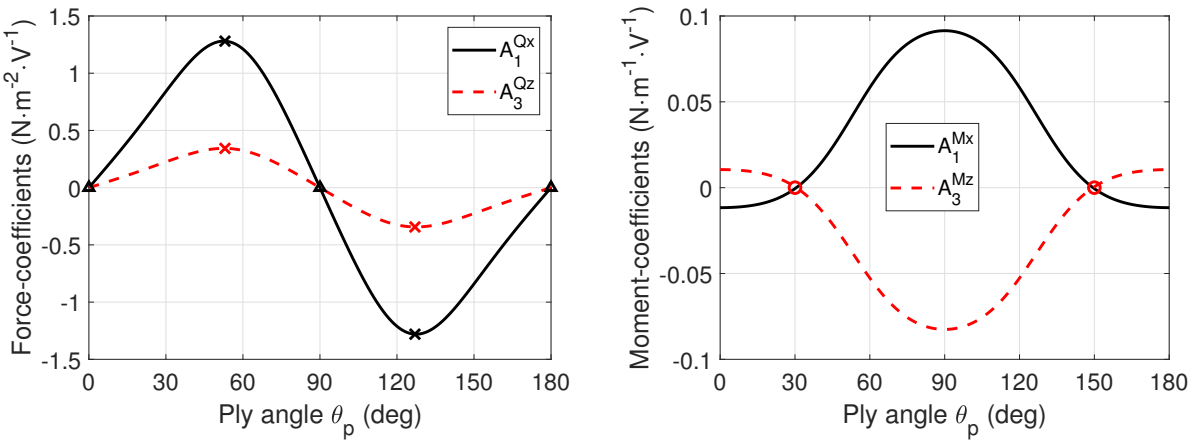

(a) $\mathcal{A}_2^{Qx}$ **&** $\mathcal{A}_4^{Qz}$ **(b)** $\mathcal{A}_1^{Mx}$ **&** $\mathcal{A}_3^{Mz}$

Fig. 5 Piezo-actuator coefficients as a function piezo-actuator ply-angle

B. Discussion of control weighting coefficients

Considering the fact that flange and web actuator-pairs are the individual actuators, the design of the associated control system can be implemented separately. The main task of the LQR controller design is determining the weighting coefficients α_K, α_M and η_i in Eq. (32). Recalling the state weighting matrix $\mathbf{Z}$ presenting in Eq. (33), two combinations of α_K and α_M are accounted, i.e., $\alpha_K = \alpha_M = 1$ for representing the total energy of the system and $\alpha_K = 0$, $\alpha_M = 1$ for representing the kinetic energy only. Fig. 6 depicts damping ratios of the first four modes as a function of η_i for the two selected α_K and α_M combinations. It can be found that damping ratios decrease with the increase of η_i. In other words, smaller control weighting coefficient η_i results higher control gain, producing greater damping ratios, implying higher voltage supplement of the control system. Therefore, the control weighting coefficients $\eta_1 = \eta_3 = 5$ are adopted for a trade off between control effectiveness and voltage supplements. In addition, on the perspective of active control of vibration suppression, it is reasonable to consider the system kinetic energy only, namely of that weighting coefficients combination $\alpha_M = 0$ and $\alpha_M = 1$ is selected for the following investigation.

In order to guarantee the accuracy of the calculation for the first four modes, adequate numbers of modes N_{mode} should be accounted in the numerical study. Fig. 7 further depicts the first four damping ratios for selected N_{mode}. It can

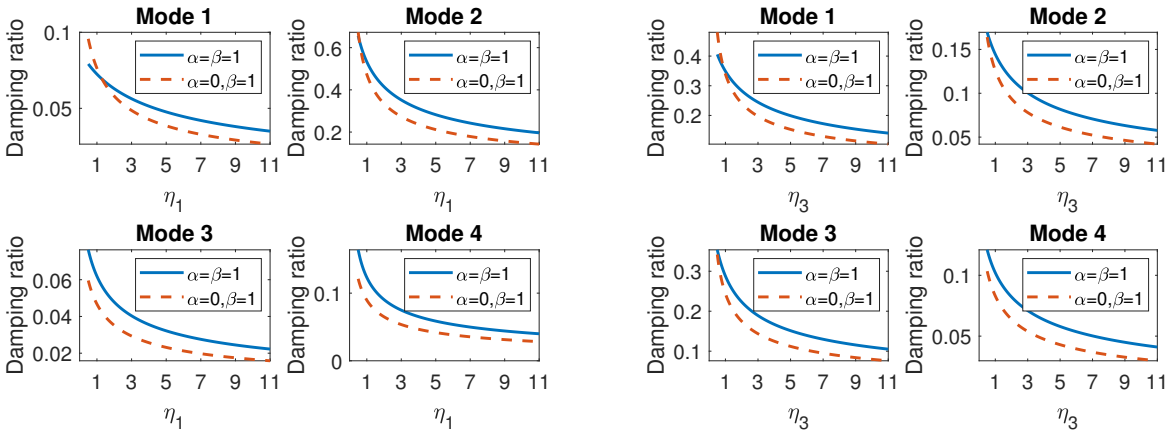

(a) Flange-actuator-pair **(b) Web-actuator-pair**

Fig. 6 Damping ratios of the first four modes versus η_i; $\beta_0 = 0°$, $\theta_h = 90°$, $\theta_p^F = \theta_p^W = 60°$

be identified that, generally, at least first six modes and first seven modes should be adopted for flange-actuator-pair in Fig. 7a and web-actuator-pair in Fig. 7b, respectively. In a nutshell, first seven modes ($N_{mode} = 7$) are accounted in the present numerical calculation after a careful examination for various host structure and piezo-actuator configurations.

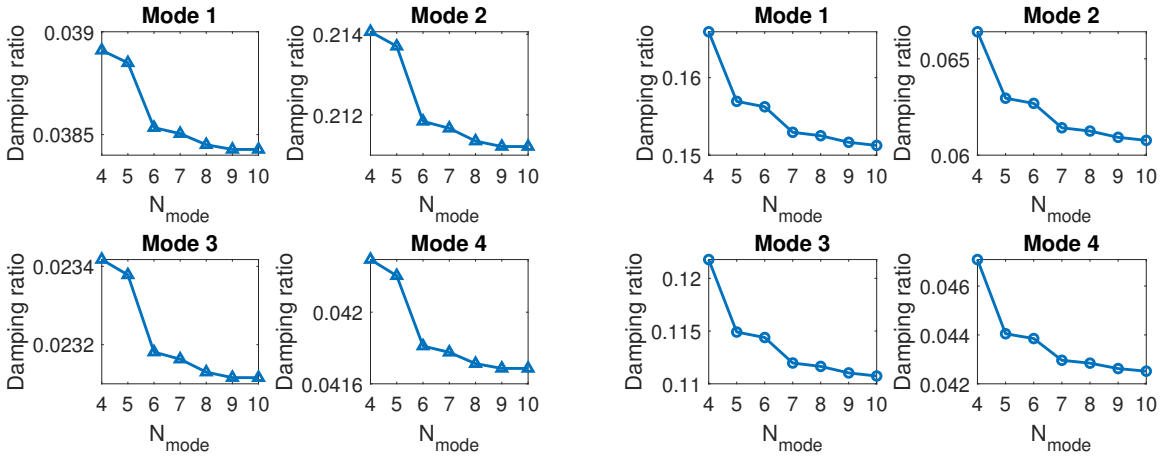

(a) Flange-actuator-pair; $\eta_1 = 5$, $\theta_p^F = 60°$ **(b) Web-actuator-pair; $\eta_3 = 5$, $\theta_W^F = 60°$**

Fig. 7 Damping ratios of the first four modes versus N_{mode}; $\beta_0 = 0°$, $\theta_h = 90°$

C. Host structure study

Influences of elastic tailoring on control authority are highlighted in Figs. 8 and 9. Actually, elastic tailoring in the present structure mainly denotes the tailoring of the bending–transverse shear couplings, namely of chordwise bending-flapwise transverse shear coupling and flapwise bending-chordwise transverse shear coupling [38]. Figs. 8 and 9 plot damping ratios induced by flange and web actuator-pairs in sequence as a function of host structure ply-angle for

selected typical actuation cases. It can be found that the control authorities contributed by piezoelectrically induced transverse shear are more sensitive to the elastic coupling compared to that contributed by piezoelectrically induced bending. In addition, in contrast to the symmetric property around $\theta_h = 90°$ of the damping ratios produced by pure bending actuations as shown in Figs. 8a and 9a, damping ratios induced by pure transverse shear actuations present non-symmetric property, especially for modes 1, 3 in Fig. 8b and modes 2, 4 in Fig. 9b. This result implies that positive or negative bending–transverse shear couplings have significant effects only on control authority induced by transverse shear actuations, considered in conjunction with the facts that the system has positive flapwise bending-chordwise transverse shear elastic coupling and negative chordwise bending-flapwise transverse shear elastic coupling in the domain $0° < \theta_h < 90°$, while has the exactly opposite elastic coupling cases in the domain $90° < \theta_h < 180°$ [35].

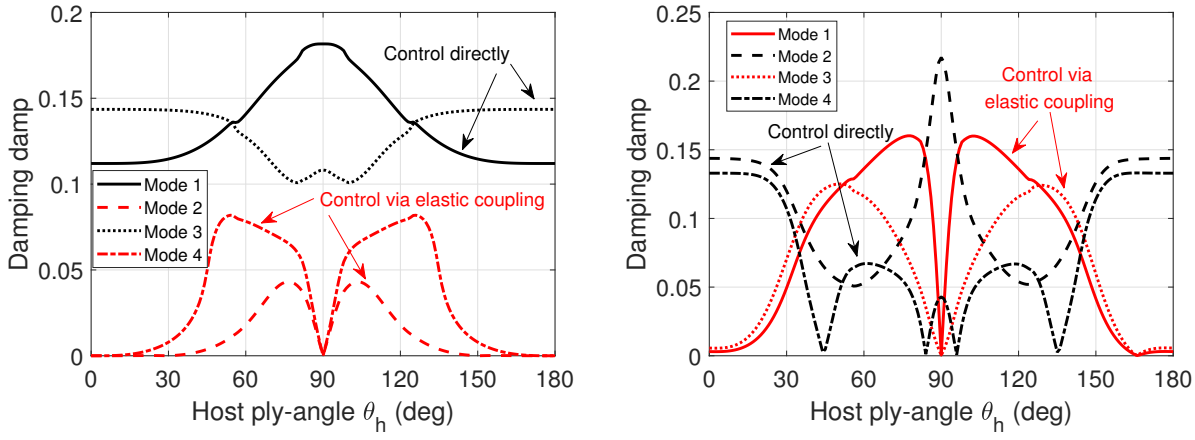

(a) Pure bending actuations; $\theta_p^F = 90°$ **(b) Pure transverse shear actuations; $\theta_p^F = 30°$**

Fig. 8 Damping ratios induced by flange-actuator-pair versus host structure ply-angle θ_h; $\beta_0 = 0°$

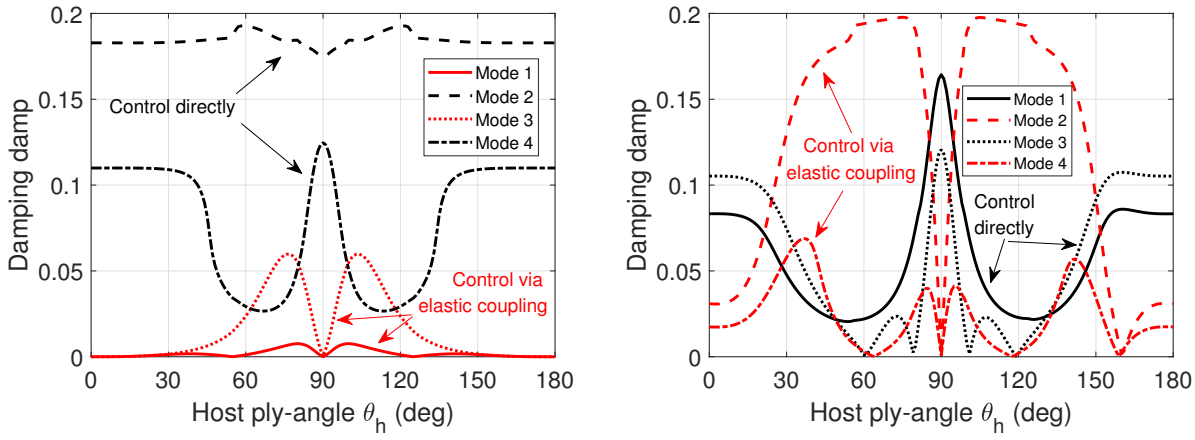

(a) Pure bending actuations; $\theta_p^W = 90°$ **(b) Pure transverse shear actuations; $\theta_p^W = 30°$**

Fig. 9 Damping ratios induced by web-actuator-pair versus host structure ply-angle θ_h; $\beta_0 = 0°$

D. Tailoring of piezo-actuators

In this section, the piezo-actuators are assumed spread over the entire beam span. As a result, the rotating blade will be controlled by piezoelectrically induced tip bending moments and inner uniform transverse shear forces. Based on the discussions in the previous section, the host structure configurations $\theta_h = 90°$ and $\theta_h = 75°$ are adopted in sequence as the weak and the strong elastic coupling cases to investigate the tailoring of the piezo-actuators for optimal active vibration control. Mode shapes of the first four modes for $\theta_h = 90°$ and $\theta_h = 75°$ cases are depicted in Figs. 10a and 10b, respectively.

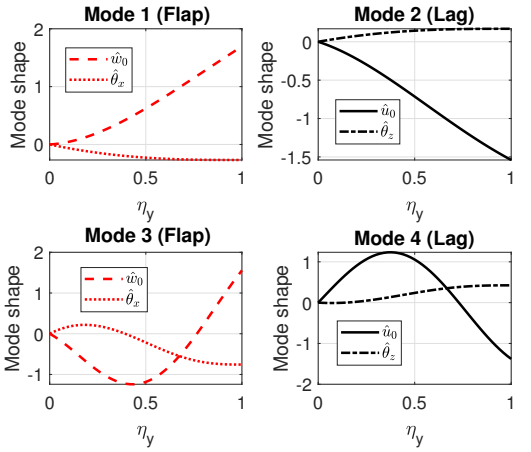

(a) Mode shapes for host structure $\theta_h = 90°$; $\beta_0 = 0°$

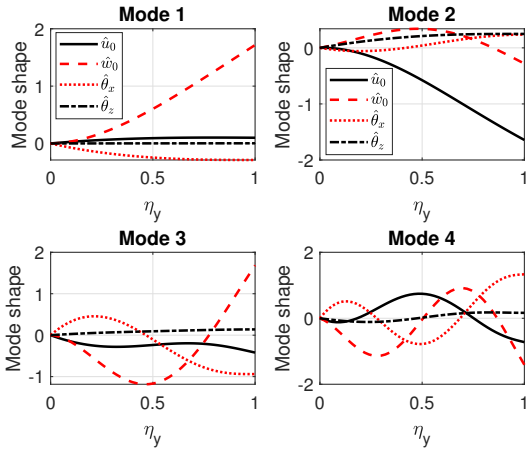

(b) Mode shapes for host structure $\theta_h = 75°$; $\beta_0 = 0°$

Fig. 10 Mode shapes of the first four modes; non-dimensional parameters are defined as $\eta_y = y/L$, $\hat{u}_0 = u_0/(2b)$, $\hat{w}_0 = w_0/(2b)$, $\hat{\theta}_x = \theta_x$, $\hat{\theta}_z = \theta_z$.

1. Un-pretwisted rotating blade

The un-pretwisted rotating blade consisting weak elastic coupling is investigated firstly. Recalling the governing equations (22)-(25), the flapwise bending (flapping motion) and chordwise bending (lagging motion) are exactly elastically decoupled for the weak elastic coupling case. Damping ratios of the first four modes plotted as a function of ply-angle of piezo-actuator are illustrated in Fig. 11. In addition, the piezoelectrically induced pure bending and pure transverses shear points are indicated by $\triangle$ and $\circ$, respectively. In fact, modes 1, 3 and modes 2, 4 are independent flapwise bending and chordwise bending modes, respectively. The result of Fig. 11a presents that flange-actuator-pair can control chordwise bending modes by piezoelectrically induced chordwise transverse shear ($\mathcal{A}_1^{Qx}$), while control flapwise bending modes by piezoelectrically induced flapwise bending ($\mathcal{A}_1^{Mx}$). It can be further found that piezoelectrically induced chordwise transverse shear will offer a similar control authority on chordwise bending modes (modes 2, 4) in the domain $10° < \theta_p^F < 70°$ or $110° < \theta_p^F < 170°$. On the contrary, piezoelectrically induced flapwise bending produces the maximum control authority only when $\theta_p^F = 90°$ or $0°, 180°$. Note that, the control authority here is optimized

on the perspective of energy consumption, in absence of the limitation of the voltages requirement. Considered in conjunction with the results of piezo-actuator coefficients in Fig. 5, in which greater absolute value of the coefficient implies lower voltage required to achieve the same actuation level, the optimal ply-angle θ_p^F is suggested to locate in the domain $53^\circ < \theta_p^F < 127^\circ$. Actually, this conclusion can be further extended for any elastic coupling cases, namely, the optimal ply-angle of flange and web actuator-pairs both should be located in the domain $53^\circ < \theta_p^F < 127^\circ$ in priority.

Similar results can also be concluded for web-actuator-pair in Fig. 11b, e.g., flapwise bending modes and chordwise bending modes can be restrained by piezoelectrically induced flapwise transverse shear ($\mathcal{A}_3^{Q_z}$) and chordwise bending ($\mathcal{A}_3^{M_z}$), respectively; piezoelectrically induced flapwise transverse shear produces a similar control authority on flapwise bending modes (modes 1, 3) in the domain $10^\circ < \theta_p^F < 50^\circ$ or $130^\circ < \theta_p^F < 170^\circ$.

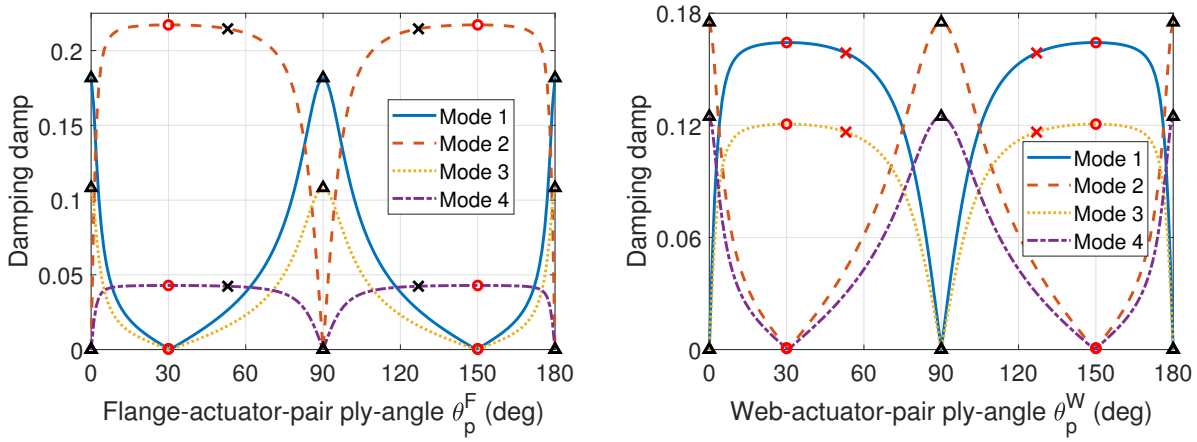

(a) Flange-actuator-pair **(b) Web-actuator-pair**

Fig. 11 Damping ratios versus θ_p for the weak elastic coupling case; $\theta_h = 90^\circ$, $\beta_0 = 0^\circ$

Figure 12a further illustrates the associate minimum cost functions J_{min} under the velocity initial condition (V-initial) for the individual mode. For example, the velocity initial condition for mode 2 is given as

$$\mathbf{x}(0) = \big[\underbrace{0\ 1\ 0\ 0\cdots}_{N_{mode}}\big|\underbrace{0\ 0\ 0\ 0\cdots}_{N_{mode}}\big]^T, \tag{40}$$

where N_{mode} denotes the first N modes that adopted in the numerical calculation. In order to estimate the control authority for the all first four modes in a holistic perspective, the minimum cost function J_{min} under the V-initial conditions of

$$\mathbf{x}(0) = \big[\underbrace{1\ 1\ 1\ 1\ 0\ 0\cdots}_{N_{mode}}\big|\underbrace{0\ 0\ 0\ 0\ 0\ 0\cdots}_{N_{mode}}\big]^T \tag{41}$$

is shown in Fig. 12b. According to the definition of the cost function, unit of J_{min} is $J{\cdot}s$. However, J_{min} presented here can be treated as a nondimensional parameter, since on one hand unit of the V-initial conditions as given in Eqs. (40)

and (41) are not specified, on the other hand J_{min} illustrates in Fig. 12 is essentially a comprehensive indicator of control effectiveness (vibration elimination time) and energy consumption. Specifically, lower minimum cost function J_{min} indicates that piezo-actuator can suppress the system vibration faster with an optimal energy consumption. Based on the results that the modes dominated by the transverse shear actuation present lowest J_{min} in a wide range domain as shown in Fig. 12a, it can be concluded that the LQR optimal control prefers to achieve the transverse shear control authority in priority at the expense of reducing the bending control authority. In addition, it can be seen from the result of Fig. 12b that both flange and web actuator-pairs can individually control the flapping and lagging motions simultaneously.

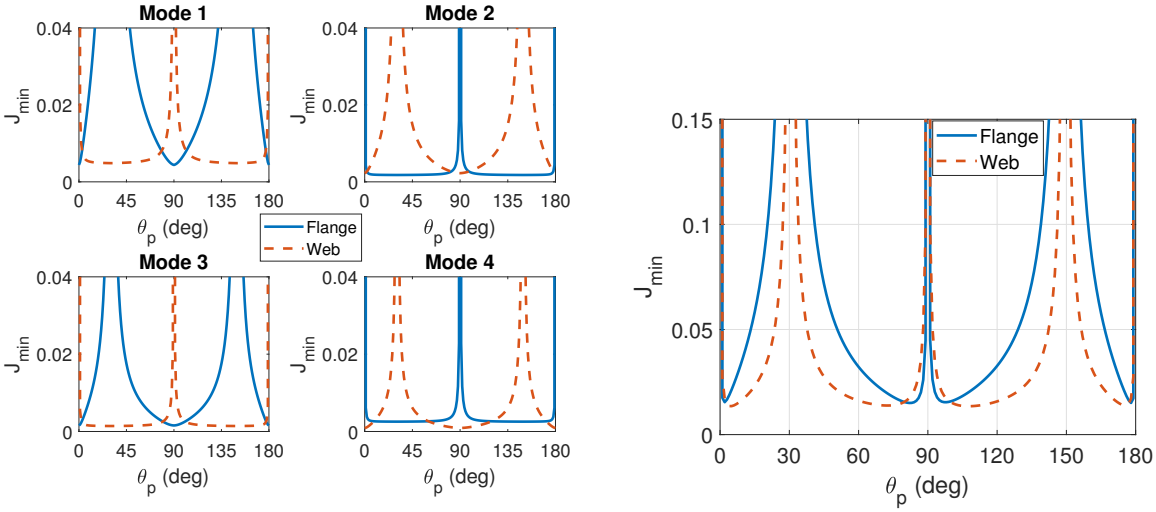

(a) V-initial condition for the individual mode **(b) V-initial condition for all the first four modes**

Fig. 12 J_{min} **versus piezo-actuator ply-angle** θ_p **for the weak elastic coupling;** $\theta_h = 90°$**,** $\beta_0 = 0°$

For the strong elastic couping case, Figs. 13a and 13b plot damping ratios of the first four modes as a function of flange-actuator-pair ply-angle θ_p^F and web-actuator-pair ply-angel θ_F^W, respectively. In Fig. 13, no matter the piezoelectrically induced pure transverse shear (indicated in ○) or pure bending (indicated in △) can individually control the flapping-lagging coupled system via the elastic coupling. It can be found that the variations of damping ratios are complicated compared to that of the weak elastic case as shown in Fig. 11. In order to capture some valuable information, Fig. 14 further depicts the associated J_{min} under the velocity initial condition. It can be seen that the first four modes present the similar J_{min} distributions when activated by the flange-actuator-pair as shown by solid lines in Fig. 14a, resulting a distinct J_{min} distribution in Fig. 14b. Thus, the optimal ply-angle of flange-actuator-pair is suggested located in the domain $90° < \theta_p^F < 127°$ in conjunction with the consideration of the voltage limitation. Whereas, for the web-actuator-pair case as shown by dashed lines in Fig. 14a, J_{min} distributions of the first four modes differ from one another, increasing the difficulty in identifying the optimal ply-angle of θ_p^W. Based on the result of Fig. 14b, $\theta_p^W \approx 65°$ can achieve the lowest J_{min} when the first four modes are all accounted. However, web-actuator-pair will lose control easily on mode 2 when $\theta_p^W \approx 69°$. Thus $\theta_p^W \approx 60°$ indicated by ⋄ in Fig. 14b is suggested for robustness consideration.

Note that, the lose control points, i.e., the points with approximate zero damping ratio or extreme large minimum cost function J_{min}, contain adequate piezoelectrically induced bending and transverse shear simultaneously. This is because when the bending actuation introduces the positive control authority, the related transverse shear actuation induces negative control authority on the lose control points, or vice versa.

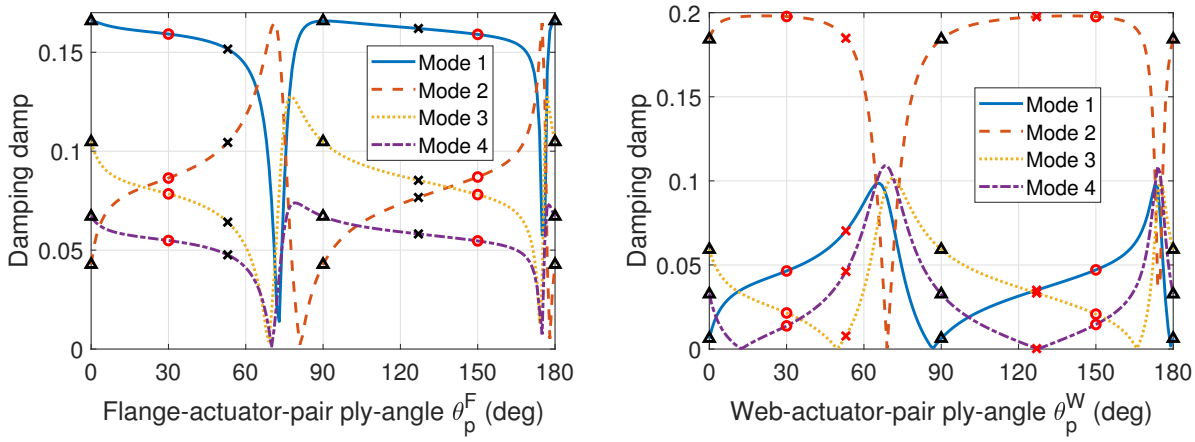

(a) Flange-actuator-pair **(b) Web-actuator-pair**

Fig. 13 Damping ratios versus θ_p for the strong elastic coupling case; $\theta_h = 75°$, $\beta_0 = 0°$

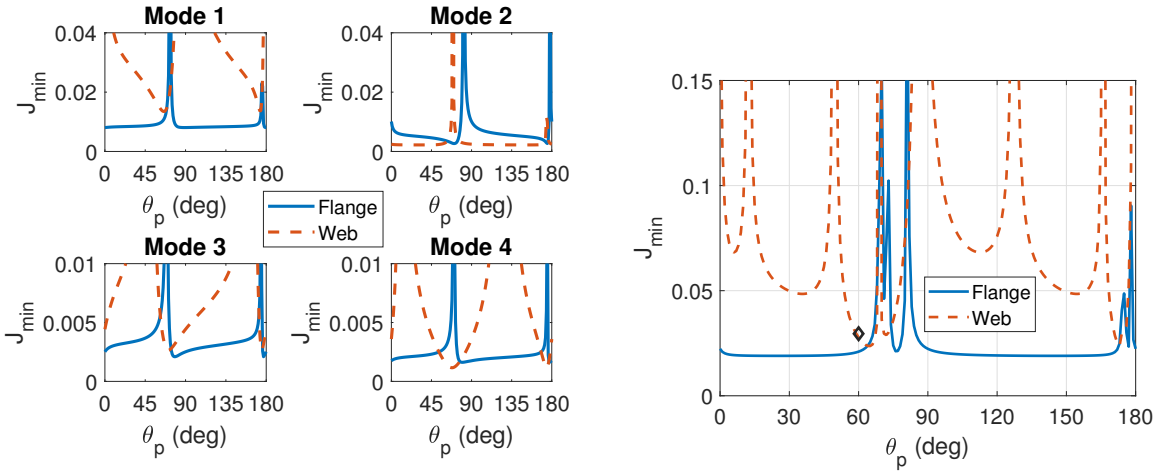

(a) V-initial condition for the individual mode **(b) V-initial condition for all the first four modes**

Fig. 14 J_{min} versus piezo-actuator ply-angle θ_p for the strong elastic coupling case; $\theta_h = 75°$, $\beta_0 = 0°$

2. Influence of pretwist angle

Pretwist angle will introduce additional couplings between the flapping and the lagging motions. Figs. 15 and 16 present control authorities of a pretwisted rotary thin-walled beam consisting weak and strong elastic couplings, respectively. By comparing the damping ratio results between Figs. 15 and 11, it can be found that the flapping-lagging

coupling effect contributed by pretwist angle is not as significant as that induced by elastic couplings on control authority, considered in conjunction with that by comparing the results between Figs. 13 and 11.

In addition, for the weak elastic coupling case, the apparent influence of pretwist angle on control authority is solely observed on mode 3 of the flange-actuator-pair in Fig. 15a and on mode 4 of web-actuator-pair in Fig. 15b, by comparing to the associated results of the un-pretwisted cases as shown in Figs. 11-14. While for the strong elastic coupling case as shown in Fig. 16, mode 2 controlled by flange-actuator-pair and modes 3, 4 controlled by web-actuator-pair will be affected by the pretwist angle.

For the weak elastic coupling case, the optimal ply-angles $\theta_p^F \approx 99^\circ$ (indicated by $\diamond$ in Fig. 15d) and $\theta_p^W \approx 127^\circ$ (maximum transverse shear actuation point indicated by $\times$ in Fig. 15d) are suggested for flange and web actuator-pairs, respectively. While for the strong elastic coupling case, $\theta_p^F \approx 90^\circ$ (pure maximum bending actuation point indicated by $\triangle$ in Fig. 16d) and $\theta_p^W \approx 60^\circ$ (indicated by $\diamond$ in Fig. 16d) are suggested. Note that, the recommended piezo-actuator configurations of the pretwisted beams are coincidence with that of the associated un-pretwisted cases.

E. Position study

Considering the high cost of the piezo-composite material, the relationship between control authority and pizo-actuator size and position should be investigated. Before we address this topic, two nondimensional parameters are defined, viz.,

$$\eta_s = \frac{y_2 - y_1}{L}, \quad \eta_p = \frac{y_1 + y_2}{2L}, \tag{42}$$

where y_1 and y_2 are used to describe the position of the piezo-actuator as shown in Fig. 1; parameter η_s denotes the piezo-actuator size; and the position parameter η_p is the distance from the blade root to the centroid of the piezo-actuator.

In fact, a comprehensive investigation of the optimization of the control authority is a difficult task, since a lot of factors should be accounted, such as pretwist and presetting angles, elastic couplings, piezoelectrically induced actuation couplings, size and position of piezo-actuators and the control strategy. Therefore, the main objective of this section is try to summarize some general rules to guide the complicated optimization process.

Before the position investigation implemented, Fig. 17 highlights the influences on piezo-actuator position study when ignoring the additional mass and stiffness of piezo-actuators. Fig. 17a plots damping ratios of the first four modes as a function of position parameter η_p when flange- and web-actuator-pairs are activated simultaneously. Note that, the solution without actuator mass and stiffness is indicated by the solid line, while the solution with them is indicated by the dashed line. It can be found that ignoring the effects of mass and stiffness of the piezo-actuators solely results in less than 7% error as shown in Fig. 17b. Thus, the effects of mass and stiffness of the piezo-actuators are ignored in the following discussions.

Figures 18-21 depict the first four damping ratios of the system as a function of position parameter η_p for selected

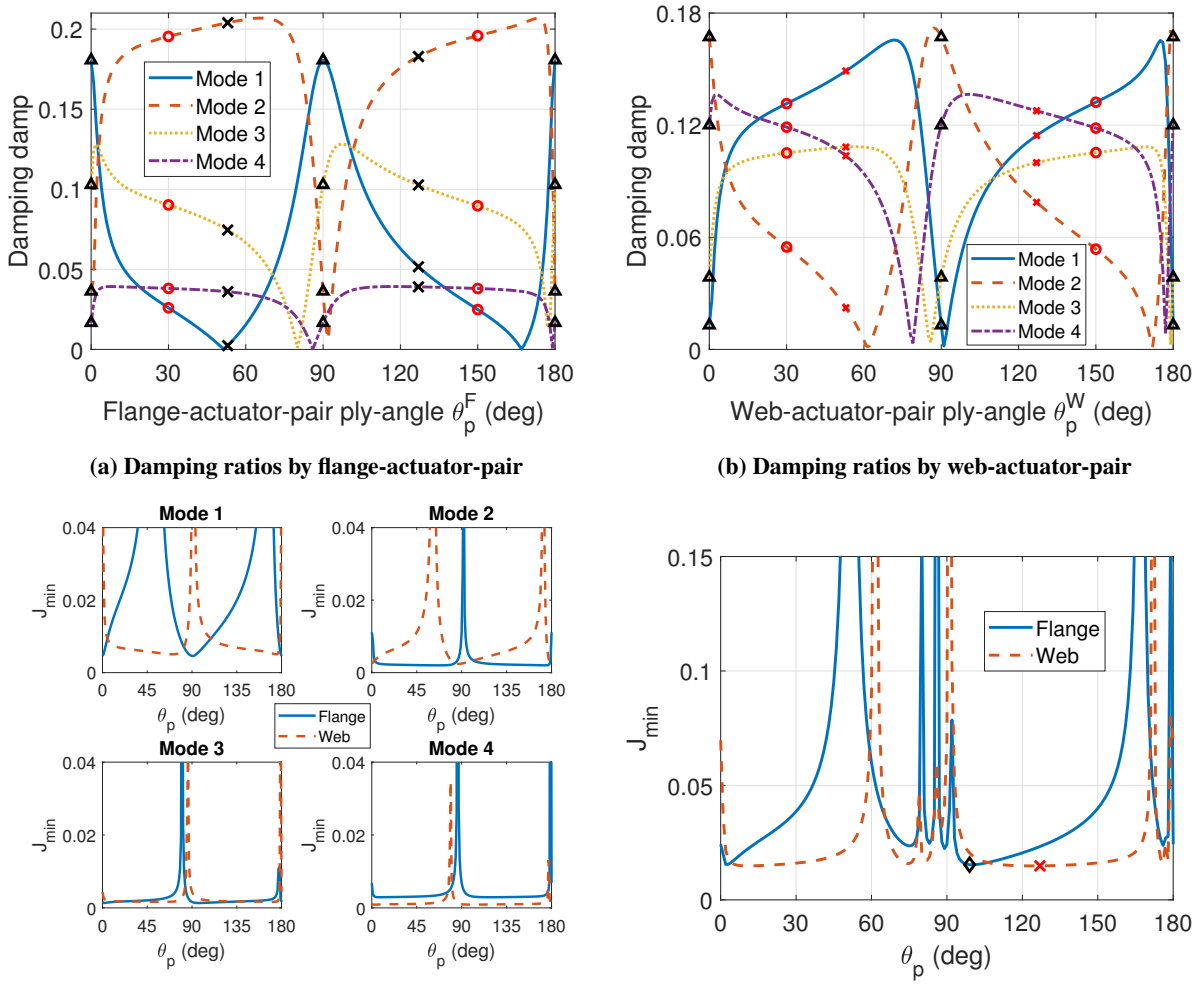

(a) Damping ratios by flange-actuator-pair

(b) Damping ratios by web-actuator-pair

(c) J_{min} for the individual mode

(d) J_{min} for all the first four modes

Fig. 15 Damping ratios and J_{min} versus θ_p for the weak elastic coupling case; $\theta_h = 90°$, $\beta_0 = 60°$

combinations of influence factors, such as the elastic coupling, the actuation coupling, the size of the piezo-actuator. Considering the facts that the flange and web actuator-pairs can control the system independently, the are discussed separately. Special attention should be paid on the piezoelectrically induced bending and transverse shear coupling case considering the evident drawbacks of either pure bending or pure transverse shear cases, i.e., pure bending case loses the directly twist control ability and pure transverse shear case requires much higher applied voltages.

The flange-actuator-pair is discussed firstly. From the result of Fig. 18, it can be found that damping ratio of mode 1 decreases when the position moves from the blade root to the tip. In other words, flange-actuator-pair produces the maximum damping ratio of mode 1 when it locates near the blade root. Whereas, its optimal position producing desirable damping ratios of modes 2 and 3 is near the middle of the span as shown in Figs. 19 and 20. The optimal position for mode 4 is hardly to determine, since the size of piezo-actuator and the elastic coupling both have significant effects on control authority of mode 4. Note that, the influence induced by piezoelectric actuation couplings seems

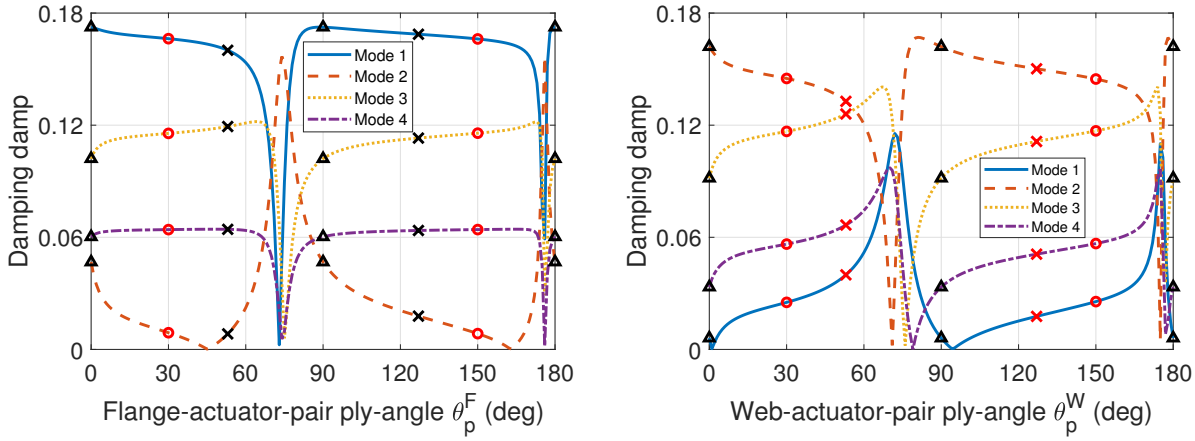

(a) Damping ratios by flange-actuator-pair **(b) Damping ratios by web-actuator-pair**

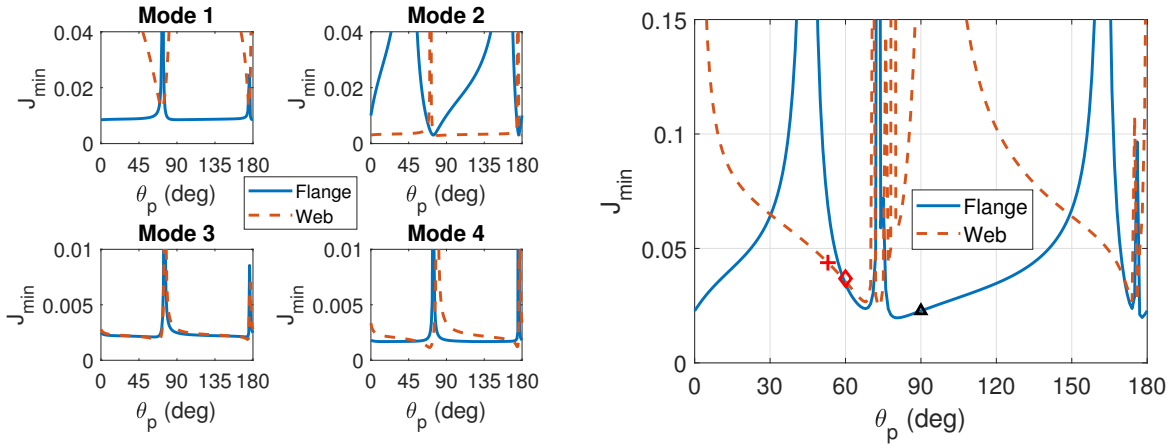

(c) J_{min} for the individual mode **(d) J_{min} for all the first four modes**

Fig. 16 Damping ratios and J_{min} versus θ_p for the strong elastic coupling case; $\theta_h = 75°$, $\beta_0 = 60°$

inconsequential for mode 4 as illustrated in Fig. 21. In conclusion, based on the results of Figs. 18-21 (indicated by black color), elastic coupling and the piezo-actuator size are the greater weight factors for the flange-actuator-pair position optimization.

As for web-actuator-pair as indicated by red color in Figs. 18-21, it can be found that the position optimization results are completely different form that of the flange-actuator-pair. The control authority on mode 1 is not sensitive to the position as shown in Fig. 18. While the control authority on mode 2 decreases when the position moves from the blade root to the tip, see Fig. 19. Whereas, according to the results in Figs. 20 and 21, the optimal position for modes 3 and 4 are significantly affected by the size, the elastic coupling, the piezoelectrically induced actuation coupling etc.

VI. Conclusions

Based on the LQR control strategy, active control of pretwisted smart blades modeled as rotating composite thin-walled beams incorporating piezo-composite is implemented. The piezo-actuators are grouped as two independent

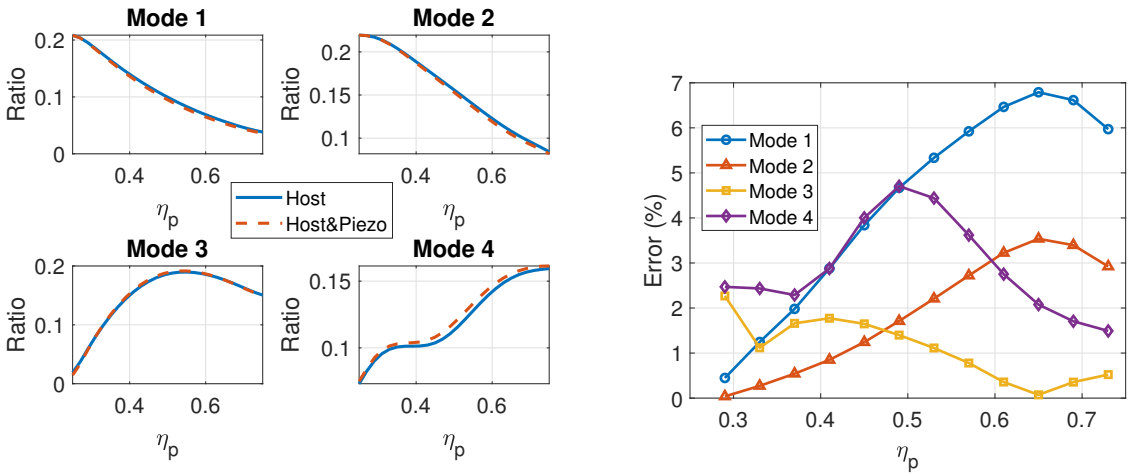

(a) Damping ratio for the first four modes; $\theta_h = 75°$, $\theta_p^F = \theta_p^W = 105°$, $\eta_s = 0.5$. **(b) Errors** $(error = \left|\frac{[Host] - [Host\&Piezo]}{[Host\&Piezo]}\right| \times 100\%)$.

Fig. 17 The influence of mass and stiffness of the piezo-actuator.

actuator-pairs, viz., flange-actuator-pair and web-actuator-pair. The synergistic effect played by the directionality property of piezo-composite layers, considered in conjunction with that of tailored fiber-reinforced host structure, on their dynamic response characteristics was highlighted. In addition, pertinent suggestions are summarized for decreasing the difficulty of the complex optimization process for the piezo-actuator placement and sizing. Considering the evident drawbacks of piezoelectrically induced either pure bending or pure transverse shear cases, i.e., pure bending case loses the directly twist control ability and pure transverse shear case requires much higher applied voltages, piezoelectrically induced transverse shear and bending coupling seems the optimal choice for active control of the flapping or lagging motion. In fact, by adjusting the weight of the piezoelectrically induced transverse shear component in the coupling, the control authority of the desirable mode can be increased at the expense of reducing that of others. In addition, the main conclusions of the present article include:

1) piezoelectrically induced transverse shear plays an important role on active control of flapping and lagging motions of the blade;
2) control authorities contributed by piezoelectrically induced transverse shears are more sensitive to the elastic coupling compared to that contributed by piezoelectrically induced bendings;
3) both flange and web actuator-pairs can individually control the flapping and lagging motions simultaneously;
4) on the perspective of energy consumption, the implemented LQR optimal control prefers to achieve the transverse shear control authority in priority at the expense of reducing the bending control authority.

Funding Sources

The authors thank to National Natural Science Foundation of China for the financial support (No. 11802120).

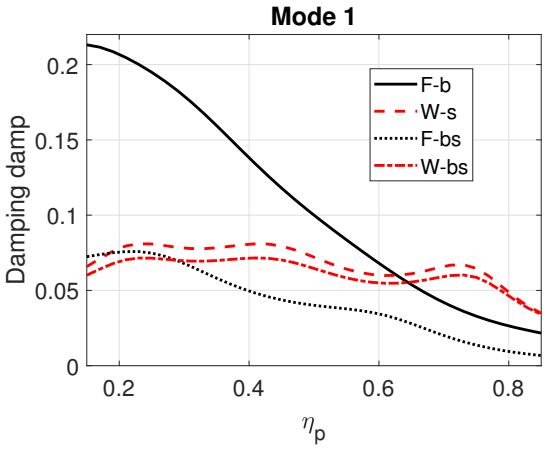

(a) **Small size** $\eta_s = 0.3$ **with weak elastic coupling** $\theta_h = 90°$

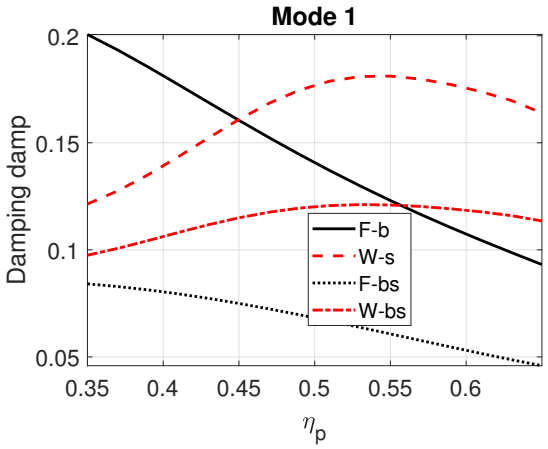

(b) **Large size** $\eta_s = 0.7$ **with weak elastic coupling** $\theta_h = 90°$

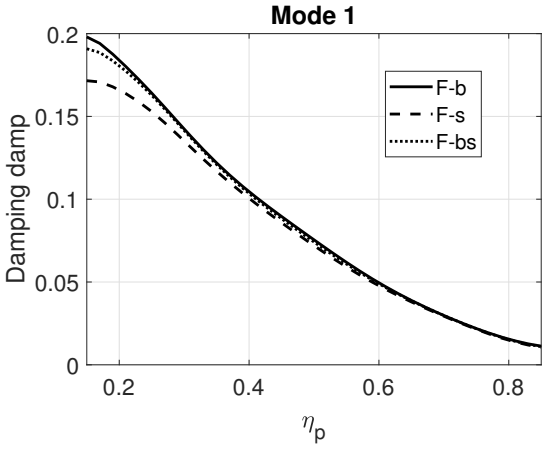

(c) **Small size** $\eta_s = 0.3$ **with weak strong coupling** $\theta_h = 75°$

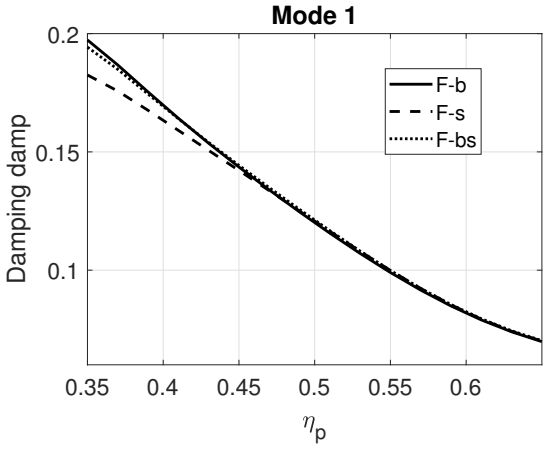

(d) **Large size** $\eta_s = 0.7$ **with weak strong coupling** $\theta_h = 75°$

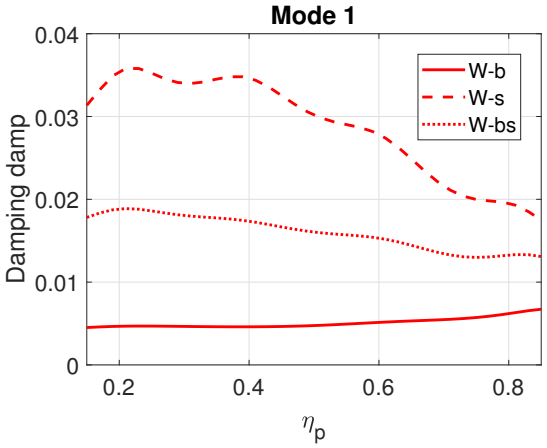

(e) **Small size** $\eta_s = 0.3$ **with weak strong coupling** $\theta_h = 75°$

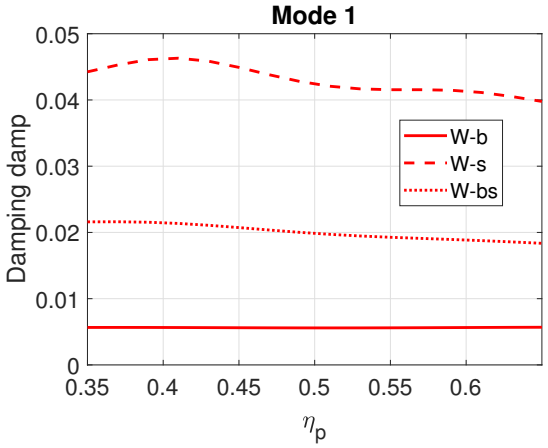

(f) **Large size** $\eta_s = 0.7$ **with weak strong coupling** $\theta_h = 75°$

Fig. 18 Damping ratio of mode 1 **versus piezo-actuator position;** $F-$ **and** $B-$**: flange and web actuator-pairs, respectively;** $-b$**,** $-s$**,** $-bs$**: pure bending (**$\theta_p = 90°$**), pure transverse shear (**$\theta_p = 150°$**), coupling actuations (**$\theta_p = 105°$**), respectively.**

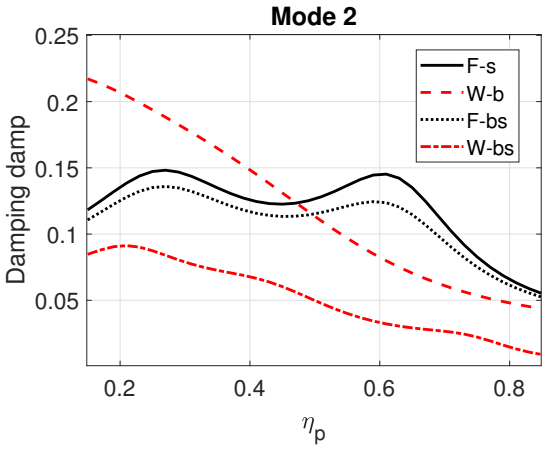

(a) small size $\eta_s = 0.3$ with weak elastic coupling $\theta_h = 90°$

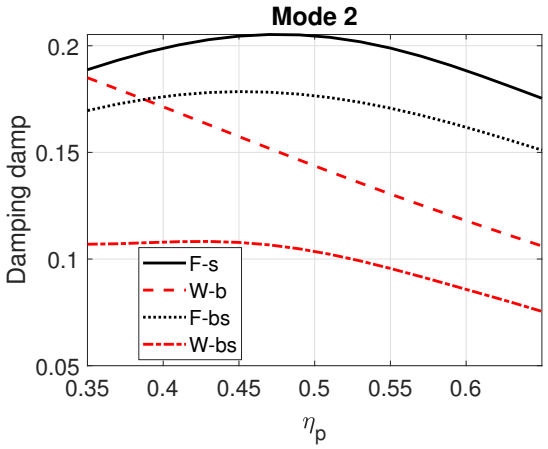

(b) Large size $\eta_s = 0.7$ with weak elastic coupling $\theta_h = 90°$

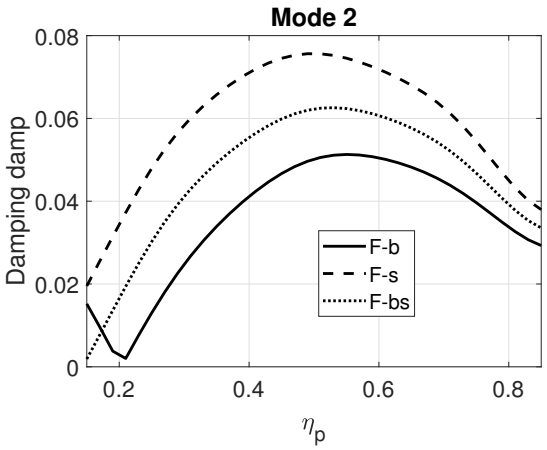

(c) Small size $\eta_s = 0.3$ with weak strong coupling $\theta_h = 75°$

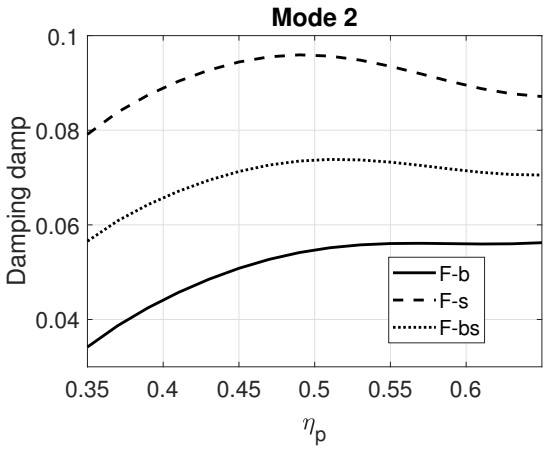

(d) Large size $\eta_s = 0.7$ with weak strong coupling $\theta_h = 75°$

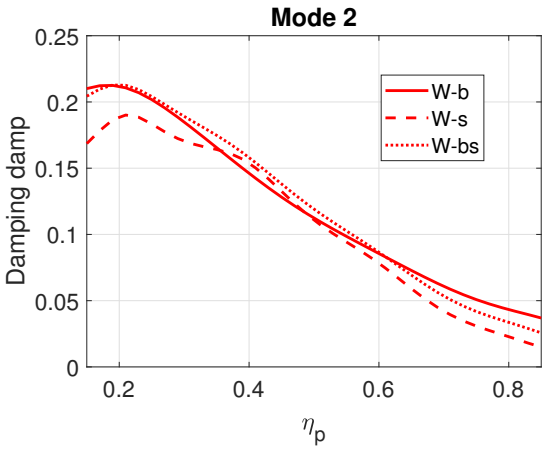

(e) Small size $\eta_s = 0.3$ with weak strong coupling $\theta_h = 75°$

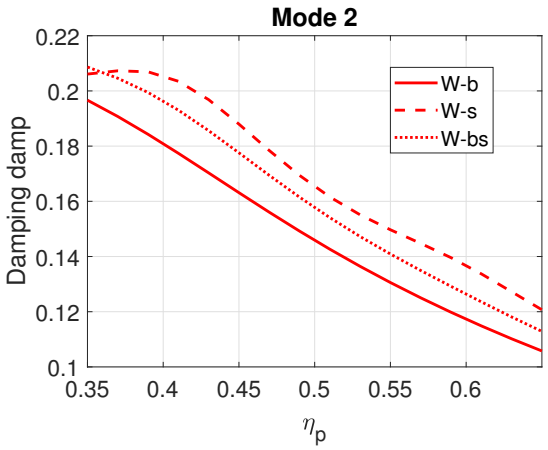

(f) Large size $\eta_s = 0.7$ with weak strong coupling $\theta_h = 75°$

Fig. 19 Damping ratio of mode 2 versus piezo-actuator position; $F-$ and $B-$: flange and web actuator-pairs, respectively; $-b$, $-s$, $-bs$: pure bending ($\theta_p = 90°$), pure transverse shear ($\theta_p = 150°$), coupling actuations ($\theta_p = 105°$), respectively.

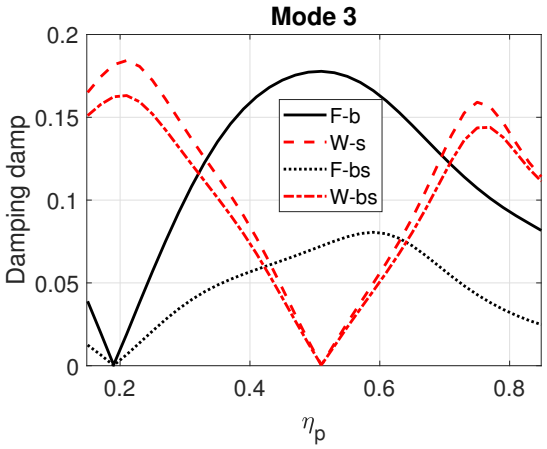

(a) small size $\eta_s = 0.3$ with weak elastic coupling $\theta_h = 90°$

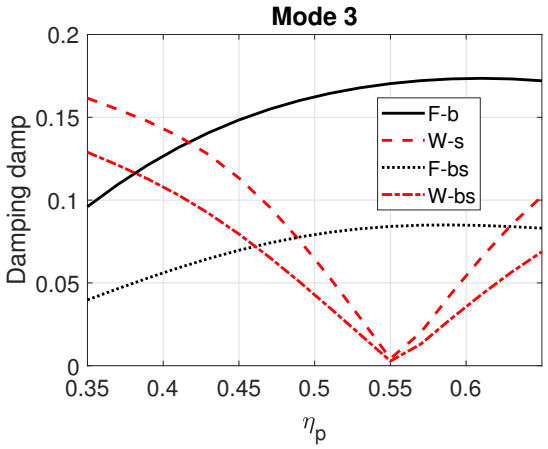

(b) Large size $\eta_s = 0.7$ with weak elastic coupling $\theta_h = 90°$

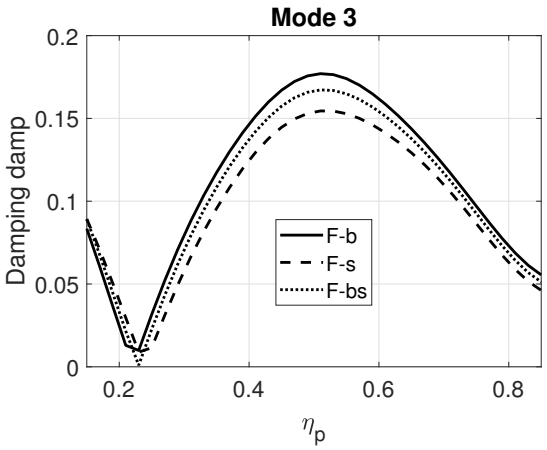

(c) Small size $\eta_s = 0.3$ with weak strong coupling $\theta_h = 75°$

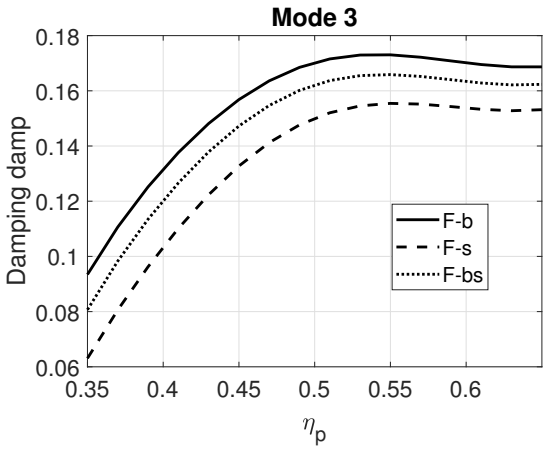

(d) Large size $\eta_s = 0.7$ with weak strong coupling $\theta_h = 75°$

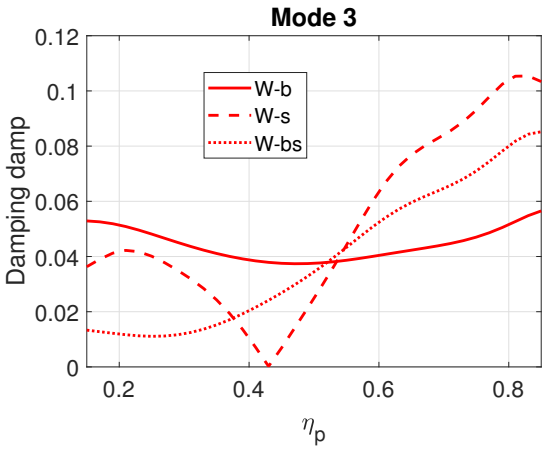

(e) Small size $\eta_s = 0.3$ with weak strong coupling $\theta_h = 75°$

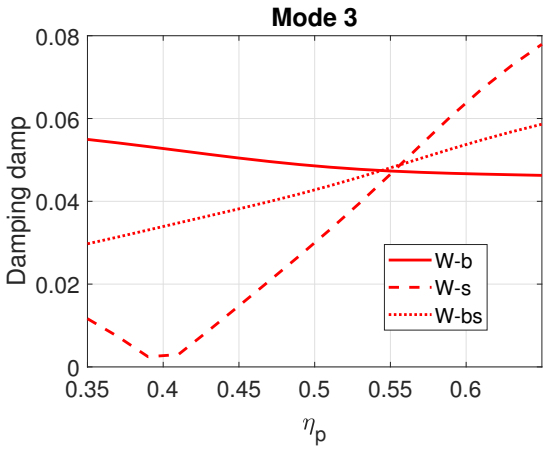

(f) Large size $\eta_s = 0.7$ with weak strong coupling $\theta_h = 75°$

Fig. 20 Damping ratio of mode 3 versus piezo-actuator position; $F-$ and $B-$: flange and web actuator-pairs, respectively; $-b$, $-s$, $-bs$: pure bending ($\theta_p = 90°$), pure transverse shear ($\theta_p = 150°$), coupling actuations ($\theta_p = 105°$), respectively.

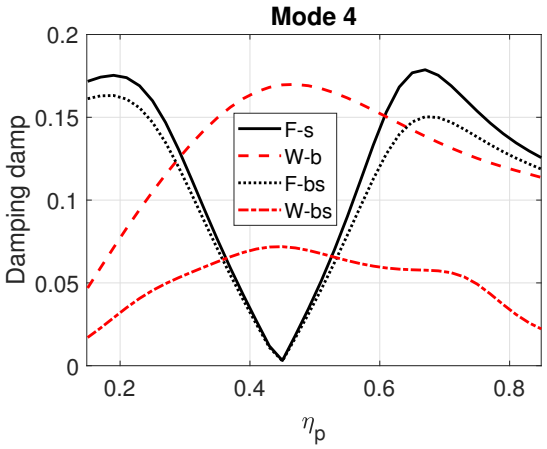

(a) small size $\eta_s = 0.3$ with weak elastic coupling $\theta_h = 90°$

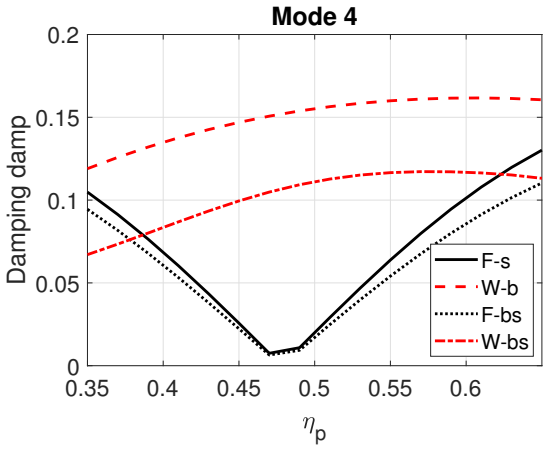

(b) Large size $\eta_s = 0.7$ with weak elastic coupling $\theta_h = 90°$

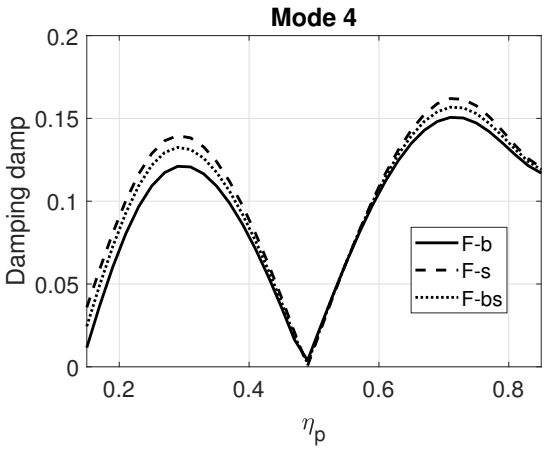

(c) Small size $\eta_s = 0.3$ with weak strong coupling $\theta_h = 75°$

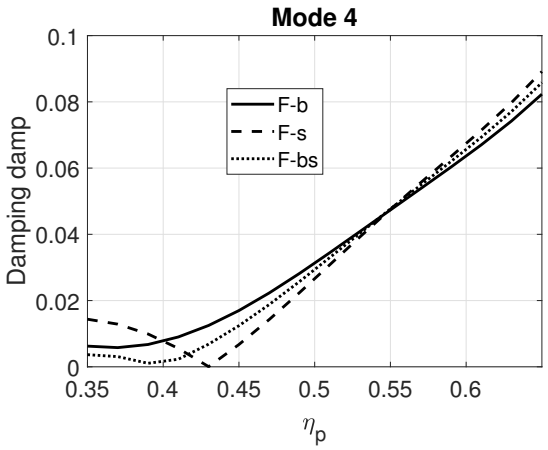

(d) Large size $\eta_s = 0.7$ with weak strong coupling $\theta_h = 75°$

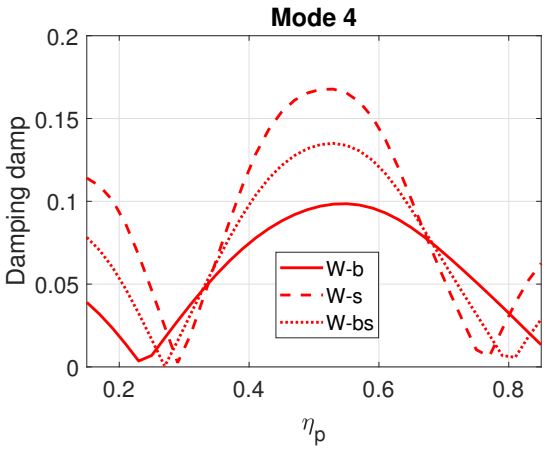

(e) Small size $\eta_s = 0.3$ with weak strong coupling $\theta_h = 75°$

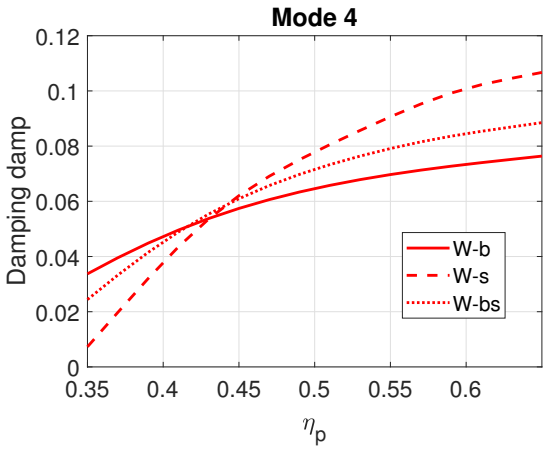

(f) Large size $\eta_s = 0.7$ with weak strong coupling $\theta_h = 75°$

Fig. 21 Damping ratio of mode 4 versus piezo-actuator position; $F-$ and $B-$: flange and web actuator-pairs, respectively; $-b$, $-s$, $-bs$: pure bending ($\theta_p = 90°$), pure transverse shear ($\theta_p = 150°$), coupling actuations ($\theta_p = 105°$), respectively.

Acknowledgments

The author Xiao Wang is indebted to Prof. Marco Morandini of Politecnico di Milano, Prof. Zhanming Qin of Xi'an Jiaotong University and Prof. Xiaoting Rui of Nanjing University of Science and Technology for their encouraging support and valuable technical advices.

References

[1] Hodges, D. H., "Review of composite rotor blade modeling," *AIAA journal*, Vol. 28, No. 3, 1990, pp. 561–565. doi: 10.2514/3.10430.

[2] Rand, O., "Analysis of composite rotor blades," *Numerical Analysis and Modelling of Composite Materials*, Springer, 1996, pp. 1–26. doi:10.1007/978-94-011-0603-0.

[3] Jung, S. N., Nagaraj, V., and Chopra, I., "Refined structural dynamics model for composite rotor blades," *AIAA journal*, Vol. 39, No. 2, 2001, pp. 339–348. doi:10.2514/2.1310.

[4] Carrera, E., Filippi, M., and Zappino, E., "Free vibration analysis of rotating composite blades via Carrera Unified Formulation," *Composite Structures*, Vol. 106, 2013, pp. 317–325. doi:10.1016/j.compstruct.2013.05.055.

[5] Demoures, F., Gay-Balmaz, F., Leyendecker, S., Ober-Blöbaum, S., Ratiu, T. S., and Weinand, Y., "Discrete variational Lie group formulation of geometrically exact beam dynamics," *Numerische Mathematik*, Vol. 130, No. 1, 2015, pp. 73–123. doi:10.1007/s00211-014-0659-4, URL `http://dx.doi.org/10.1007/s00211-014-0659-4`.

[6] Rehfield, L. W., Atilgan, A. R., and Hodges, D. H., "Nonclassical Behavior of Thin-Walled Composite Beams with Closed Cross Sections," *Journal of the American Helicopter Society*, Vol. 35, No. 2, 1990, pp. 42–50. doi:10.4050/JAHS.35.42.

[7] Chandra, R., and Chopra, I., "Experimental-theoretical investigation of the vibration characteristics of rotating composite box beams," *Journal of Aircraft*, Vol. 29, No. 4, 1992, pp. 657–664. doi:10.2514/3.46216.

[8] Song, O., and Librescu, L., "Structural Modeling and Free Vibration Analysis of Rotating Composite Thin-Walled Beams," *Journal of the American Helicopter Society*, Vol. 42, No. 4, 1997, pp. 358–369. doi:10.4050/JAHS.42.358.

[9] Song, O., Jeong, N.-H., and Librescu, L., "Vibration and stability of pretwisted spinning thin-walled composite beams featuring bending–bending elastic coupling," *Journal of Sound and Vibration*, Vol. 237, No. 3, 2000, pp. 513–533. doi: 10.1006/jsvi.2000.3100.

[10] Oh, S.-Y., Song, O., and Librescu, L., "Effects of pretwist and presetting on coupled bending vibrations of rotating thin-walled composite beams," *Int. J. Solids Struct.*, Vol. 40, No. 5, 2003, pp. 1203–1224. doi:10.1016/S0020-7683(02)00605-4.

[11] Oh, S.-Y., Librescu, L., and Song, O., "Modelling and vibration of composite thin-walled rotating blades featuring extension-twist elastic coupling," *Aeronautical Journal*, Vol. 109, No. 1095, 2005, pp. 233–246. doi:10.1017/S0001924000005212.

[12] Ghiringhelli, G. L., Masarati, P., Morandini, M., and Muffo, D., "Integrated aeroservoelastic analysis of induced strain rotor blades," *Mechanics of Advanced Materials and Structures*, Vol. 15, No. 3-4, 2008, pp. 291–306. doi:10.1080/15376490801907822.

[13] Brillante, C., Morandini, M., and Mantegazza, P., "Periodic controllers for vibration reduction using actively twisted blades," *The Aeronautical Journal*, Vol. 120, No. 1233, 2016, pp. 1763–1784. doi:10.1017/aer.2016.80, URL https://www.cambridge.org/core/journals/aeronautical-journal/article/div-classtitleperiodic-controllers-for-vibration-reduction-using-actively-twisted-bladesdiv/89330CE640F7C750DE4FF561D31DF3D4.

[14] Glukhikh, S., Barkanov, E., Kovalev, A., Masarati, P., Morandini, M., Riemenschneider, J., and Wierach, P., "Design of helicopter rotor blades with actuators made of a piezomacrofiber composite," *Mechanics of Composite Materials*, Vol. 44, No. 1, 2008, pp. 57–64. doi:10.1007/s11029-008-0007-9.

[15] Masarati, P., and Ghiringhelli, G. L., "Characterization of anisotropic, non-homogeneous plates with piezoelectric inclusions," *Computers & Structures*, Vol. 83, No. 15-16, 2005, pp. 1171–1190. doi:10.1016/j.compstruc.2004.10.017, URL http://www.sciencedirect.com/science/article/B6V28-4FKY8WG-1/2/c4da0f3cbc7e9cbd655e84b284c805c8.

[16] Chopra, I., "Review of state of art of smart structures and integrated systems," *AIAA journal*, Vol. 40, No. 11, 2002, pp. 2145–2187. doi:10.2514/2.1561.

[17] Rafiee, M., Nitzsche, F., and Labrosse, M., "Dynamics, vibration and control of rotating composite beams and blades: A critical review," *Thin-Walled Structures*, Vol. 119, 2017, pp. 795–819. doi:10.1016/j.tws.2017.06.018.

[18] Park, S.-E., and Shrout, T. R., "Ultrahigh strain and piezoelectric behavior in relaxor based ferroelectric single crystals," *Journal of Applied Physics*, Vol. 82, No. 4, 1997, pp. 1804–1811. doi:10.1063/1.365983.

[19] Bent, A. A., Hagood, N. W., and Rodgers, J. P., "Anisotropic actuation with piezoelectric fiber composites," *Journal of Intelligent Material Systems and Structures*, Vol. 6, No. 3, 1995, pp. 338–349. doi:10.1177/1045389X9500600305.

[20] WK, W., and KC, P., "An aeroelastic analysis of helicopter rotor blades incorporating piezoelectric fiber composite twist actuation," 1996.

[21] Chee, C. Y., Tong, L., and Steven, G. P., "A review on the modelling of piezoelectric sensors and actuators incorporated in intelligent structures," *Journal of Intelligent Material Systems and Structures*, Vol. 9, No. 1, 1998, pp. 3–19. doi:10.1177/1045389X9800900101.

[22] Song, O., and Librescu, L., "Modeling and dynamic behavior of rotating blades carrying a tip mass and incorporating adaptive capabilities," *Acta Mechanica*, Vol. 134, No. 3-4, 1999, pp. 169–197. doi:10.1007/BF01312654.

[23] Shim, J. K., and Na, S., "Modeling and vibration feedback control of rotating tapered composite thin-walled blade," *KSME international journal*, Vol. 17, No. 3, 2003, p. 380. doi:10.1007/BF02984364.

[24] Na, S., Librescu, L., and Shim, J. K., "Modeling and bending vibration control of nonuniform thin-walled rotating beams incorporating adaptive capabilities," *International Journal of Mechanical Sciences*, Vol. 45, No. 8, 2003, pp. 1347–1367. doi:10.1016/j.ijmecsci.2003.09.015.

[25] Na, S., and Librescu, L., "Oscillation control of cantilevers via smart materials technology and optimal feedback control: actuator location and power consumption issues," *Smart Materials and Structures*, Vol. 7, No. 6, 1998, p. 833. doi: 10.1088/0964-1726/7/6/011.

[26] Na, S., Librescu, L., Kim, M.-H., Jeong, I.-J., and Marzocca, P., "Robust aeroelastic control of flapped wing systems using a sliding mode observer," *Aerosp. Sci. Technol.*, Vol. 10, No. 2, 2006, pp. 120–126. doi:10.1016/j.ast.2005.10.002.

[27] Choi, S.-C., Park, J.-S., and Kim, J.-H., "Vibration control of pre-twisted rotating composite thin-walled beams with piezoelectric fiber composites," *J. Sound Vib.*, Vol. 300, No. 1, 2007, pp. 176–196. doi:10.1016/j.jsv.2006.07.051.

[28] Librescu, L., Na, S., Qin, Z., and Lee, B., "Active aeroelastic control of aircraft composite wings impacted by explosive blasts," *J. Sound Vib.*, Vol. 318, No. 1, 2008, pp. 74–92. doi:10.1016/j.jsv.2008.04.007.

[29] Cha, S.-J., Song, J.-S., Lee, H.-H., Na, S., Shim, J.-H., and Marzocca, P., "Dynamic response control of rotating thin-walled composite blade exposed to external excitations," *J. Aerosp. Eng.*, Vol. 27, No. 5, 2014, p. 04014025. doi:10.1061/(ASCE)AS. 1943-5525.0000335.

[30] Song, O., Librescu, L., and Oh, S.-Y., "Vibration of pretwisted adaptive rotating blades modeled as anisotropic thin-walled beams," *AIAA journal*, Vol. 39, No. 2, 2001, pp. 285–295. doi:10.2514/2.1303.

[31] Shete, C., Chandiramani, N., and Librescu, L., "Optimal control of a pretwisted shearable smart composite rotating beam," *Acta Mechanica*, Vol. 191, No. 1-2, 2007, pp. 37–58. doi:10.1007/s00707-007-0443-y.

[32] Chandiramani, N., "Active control of a piezo-composite rotating beam using coupled plant dynamics," *Journal of Sound and Vibration*, Vol. 329, No. 14, 2010, pp. 2716–2737. doi:10.1016/j.jsv.2010.01.023.

[33] Chattopadhyay, A., Gu, H., and Liu, Q., "Modeling of smart composite box beams with nonlinear induced strain," *Composites Part B: Engineering*, Vol. 30, No. 6, 1999, pp. 603–612. doi:10.1016/S1359-8368(99)00019-0.

[34] Chattopadhyay, A., Liu, Q., and Gu, H., "Vibration reduction in rotor blades using active composite box beam," *AIAA journal*, Vol. 38, No. 7, 2000, pp. 1125–1131. doi:10.2514/2.1097.

[35] "Modeling and control for rotating pretwisted thin-walled beams with piezo-composite," *Composite Structures*, Vol. 180, 2017, pp. 647 – 663. doi:10.1016/j.compstruct.2017.08.041.

[36] Kielb, R., "Effects of warping and pretwist on torsional vibration of rotating beams," *Journal of applied mechanics*, Vol. 51, 1984, p. 913. doi:10.1115/1.3167746.

[37] Wang, X., and Qin, Z., "Nonlinear modal interactions in composite thin-walled beam structures with simultaneous 1:2 internal and 1:1 external resonances," *Nonlinear Dynamics*, Vol. 86, No. 2, 2016, pp. 1381–1405. doi:10.1007/s11071-016-2970-3, URL http://dx.doi.org/10.1007/s11071-016-2970-3.

[38] Qin, Z., and Librescu, L., "On a shear-deformable theory of anisotropic thin-walled beams: further contribution and validation," *Compos. Struct.*, Vol. 56, No. 4, 2002, pp. 345–358. doi:10.1016/S0263-8223(02)00019-3.

[39] Wilkie, W. K., Bryant, R. G., High, J. W., Fox, R. L., Hellbaum, R. F., Jalink Jr, A., Little, B. D., and Mirick, P. H., "Low-cost piezocomposite actuator for structural control applications," *SPIE's 7th Annual International Symposium on Smart Structures and Materials*, International Society for Optics and Photonics, 2000, pp. 323–334. doi:10.1117/12.388175.

[40] Wang, X., Morandini, M., and Masarati, P., "Velocity feedback damping of piezo-actuated wings," *Composite Structures*, Vol. 174, 2017, pp. 221 – 232. doi:https://doi.org/10.1016/j.compstruct.2017.04.016, URL http://www.sciencedirect.com/science/article/pii/S0263822317304233.

[41] Librescu, L., and Song, O., *Thin-Walled Composite Beams: Theory and Application*, Springer, New York, 2006. Chap.8, pp. 213-232.

[42] Rehfield, L. W., and Atilgan, A. R., "Toward understanding the tailoring mechanisms for thin-walled composite tubular beams," *Proceedings of the First USSR-US Symposium on Mechanics of Composite Materials, Riga, Latvia, May*, 1989, pp. 23–26.

[43] Palazotto, A., and Linnemann, P., "Vibration and buckling characteristics of composite cylindrical panels incorporating the effects of a higher order shear theory," *Int. J. Solids Struct.*, Vol. 28, No. 3, 1991, pp. 341–361. doi:10.1016/0020-7683(91)90198-O.

[44] Librescu, L., Meirovitch, L., and Na, S. S., "Control of cantilever vibration via structural tailoring and adaptive materials," *AIAA journal*, Vol. 35, No. 8, 1997, pp. 1309–1315. doi:10.2514/2.262.

[45] Subrahmanyam, K., and Kaza, K., "Vibration and buckling of rotating, pretwisted, preconed beams including Coriolis effects," *Journal of vibration, acoustics, stress, and reliability in design*, Vol. 108, No. 2, 1986, pp. 140–149. doi:10.1115/1.3269314.

[46] Belvin, W. K., and Park, K., "Structural tailoring and feedback control synthesis-An interdisciplinary approach," *Journal of Guidance, Control, and Dynamics*, Vol. 13, No. 3, 1990, pp. 424–429. doi:10.2514/3.25354.

[47] Park, J.-S., and Kim, J.-H., "Analytical development of single crystal Macro Fiber Composite actuators for active twist rotor blades," *Smart Mater. Struct.*, Vol. 14, No. 4, 2005, p. 745. doi:10.1088/0964-1726/14/4/033.

[48] Williams, R. B., Inman, D. J., Schultz, M. R., Hyer, M. W., and Wilkie, W. K., "Nonlinear tensile and shear behavior of macro fiber composite actuators," *Journal of Composite Materials*, Vol. 38, No. 10, 2004, pp. 855–869. doi:10.1177/0021998304040555.